

Numerical simulation of bubble deformation and breakup under simple linear shear flows

Mitsuhiko Ohta^{a,b,*}, Tetsuya Ueta^b, Yozo Toei^c, Edwin Jimenez^d, Mark Sussman^e

^a*Department of Mechanical Science, Graduate School of Technology, Industrial and Social Sciences, Tokushima University, 2-1 Minamijyousanjima-cho, Tokushima 770-8506, Japan*

^b*Department of Mechanical Engineering, Graduate School of Technology, Industrial and Social Sciences, Tokushima University, 2-1 Minamijyousanjima-cho, Tokushima 770-8506, Japan*

^c*High Performance Plastics Company, Sekisui Chemical Co., Ltd., 2-1 Hyakuyama, Mishimagun Shimamoto-cho, Osaka 618-0021, Japan*

^d*Spectral Numerical, LLC, 1942 Broadway St., STE 314C, Boulder, CO 80302, USA*

^e*Department of Mathematics, Florida State University, Tallahassee, FL 32306, USA*

Abstract

For the first time, either experimentally or numerically, numerical simulations are presented for the deformation and breakup of a bubble in liquids undergoing simple linear shear flow in the low Capillary number, high Reynolds number regime. Numerical results are obtained using a projection method for incompressible two-phase flow. The method represents interfaces using the sharp interface coupled level set and Volume-Of-Fluid (CLSVOF) method. To verify our numerical algorithm and provide a basis for comparison, we also present simulation results that compare with previous, more popular, drop deformation and rupture simulations. The numerical results reveal that the shear-induced bubble deformation and breakup process differs significantly from that of the analogous drop system under similar flow conditions. The first distinguishing factor for bubble breakup is that the magnitude of shear flow necessary for causing rupture is much larger than that in the drop system case. In other words, a larger Reynolds number is needed to induce bubble breakup. The second distinct feature of the bubble system versus the drop system is that the bubble does not maintain a stable deformed shape as the system parameters approach the critical “breakup” Reynolds number. It is asserted that the differences in morphology for a bubble undergoing breakup versus a drop in the same process can be attributed to the density and viscosity ratio of the corresponding two-phase flow systems. The critical conditions for bubble breakup with respect to the Reynolds and capillary numbers are determined for several cases.

Keywords: Bubble deformation, bubble breakup, shear flow, CFD

*Corresponding author: m-ohta@tokushima-u.ac.jp

1 **1. Introduction**

2 Bubble dynamics in shear flow, including breakup, is critically important
3 for various gas-liquid scientific and engineering processes. We refer the reader
4 to the following experimental studies relating to bubble deformation in foaming
5 processes, microfluidic devices, microbubbles in the blood circulation system,
6 materials processing, pharmaceuticals, minerals engineering, bubble column re-
7 actor, underwater projectiles, polyethylene devolatilization, microfluidics, food
8 aeration, and cosmetics[6, 31, 4, 10, 11, 61, 12, 65, 5, 16, 64, 14, 15, 30, 47,
9 46]. In particular, it is the study of bubble deformation as it pertains to high-
10 performance plastics applications that motivate this work.

11 This article presents computational studies of shear-driven deformation and
12 breakup of a bubble in insoluble viscous liquids. Studying bubble break-up,
13 in which we focus only on the balance of the wall driving force and bubble
14 surface tension force, via computation rather than experiments simplifies the
15 process of setting a combination of precise, simple shear flow conditions, low
16 Capillary number ($Ca = \mu_m U / \sigma$) conditions, high Reynolds' number conditions
17 ($Re = \rho_m R U / \mu_m$), low-density ratio, low viscosity ratios, and zero buoyancy ef-
18 fects. We remark that previous controlled experimental studies on shear-driven
19 bubble deformation are restricted to the low Reynolds' number and large capil-
20 lary number regime[45, 5]. One reason is that buoyancy effects are minimized in
21 highly viscous liquids. On the other hand, many applications are characterized
22 by liquids in the high Reynolds' number regime. The physical properties that
23 distinguish bubble and drop studies are expressed in terms of the density ratio
24 $\lambda = \rho_b / \rho_m$ and the viscosity ratio $\eta = \mu_b / \mu_m$, where ρ is the fluid density, μ is
25 the viscosity and the subscripts "b" and "m" denote the "bubble" or "drop" and
26 the "matrix fluid", respectively. For a bubble in an insoluble, viscous liquid,
27 $\lambda \simeq 0$ and $\eta \simeq 0$, whereas most studies dealing with a drop in an immiscible
28 viscous liquid take $\lambda = 1$ and $\eta \simeq 1$.

29 In this work, we focus on identifying critical flow states numerically, in terms
30 of dimensionless quantities, that specify the extreme conditions at which a bub-
31 ble in shear flow first transitions from deformation to breakup. We validate our
32 numerical method by examining the sensitivity of the critical bubble deforma-
33 tion and break-up flow states with respect to the grid size. We also compare
34 with previous experimental results where the experimental data is available (the
35 high Capillary number low Reynolds' number regime). An advantage of study-
36 ing shear-driven bubble deformation and breakup computationally rather than
37 experimentally is that we can easily modify bubble/drop shape initial conditions
38 [34], the gravity force term, fluid physical properties, and the geometry of the
39 (virtual) apparatus. In our computations, the time-evolution of the boundary
40 between gas and liquid is tracked with a Coupled-Level-Set and Volume-Of-
41 Fluid (CLSVOF) sharp interface capturing algorithm [53, 55]. The rationale
42 for the CLSVOF method is that the hybrid method represents the (complex)
43 gas-liquid interfaces with minimal volume loss (property of the Volume-Of-Fluid
44 method) and minimal error in the approximation of the surface tension force
45 (property of the Level-Set method). Our sharp interface approach[55, 51, 24]

46 enables us to simulate multiphase flows without artificially giving the interface
47 an empirical thickness.

48 We focus on determining critical physical conditions in which the breakup of
49 a bubble occurs in shear flow because it is important to identify the parameter
50 regimes in which a relatively simple system transitions from stable to unstable.
51 Specifically, we ascertain the critical Reynolds number (Re_c) corresponding to
52 the bubble breakup onset condition as a function of Ca .

53 In previous experimental or computational studies on the motion of bubble
54 deformation in a simple shear flow [5, 45, 31], only findings for bubble defor-
55 mation under very low Re number conditions ($Re \ll 1$) have been reported.
56 This is understandable since a low Reynolds number matrix fluid mitigates the
57 effect of gravity on distorting the comparison with the drop case. In the results
58 reported in [5], the $x - z$ cross section of the deforming bubble was close to
59 spherical in their experiments. Also in the experiments in [5], the $x - z$ cross
60 section shows minimal overall bubble rise speed in the (very) viscous fluid in
61 comparison to the rate that the bubble deforms in the $y - z$ cross section. This
62 is expected since the experiments designed by [5] closely followed the following
63 basic assumptions: (i) “steady creeping flow with negligible inertial effects,” (ii)
64 “Incompressible Newtonian fluids,” (iii) “No buoyancy effects,” (iv) “No wall
65 effects.” In this work, we determine, for the first time, the critical Reynolds
66 number ($Re \gg 1$) that leads to bubble breakup. Additionally, our computa-
67 tional studies reveal characteristics that distinguish a drop’s deformation and
68 breakup processes versus those of a bubble.

69 We remark that there have been a number of computational articles on
70 the study of lift of slightly deformable bubbles[13, 28]. We reiterate, though,
71 that for bubble deformation and breakup in shear flows, only a few articles
72 exist: [63, 62, 48]. These previous studies mainly examined the dynamics (e.g.,
73 rotation angle) of bubble deformation in shear flow. Concerning bubble breakup,
74 Wei et al. [63] presented one numerical result for a bubble breakup process
75 under the condition of Ca (capillary number) = 35. Sharifi et al[48] presented
76 two results for bubble breakup corresponding to $Ca = 7.5$ and $Ca = 11.2$. We
77 point out that all of the previous computational research on bubble deformation
78 (and breakup) under shear driven flow[63, 62, 48] use the (explicit) Lattice
79 Boltzmann method. For accurately computing the tensile strength of a bubble,
80 and accurately computing threshold parameters for break-up (what we do in this
81 article, and what was not done in previous work), it is critical that a numerical
82 method directly enforces the velocity continuity condition and the gas-liquid
83 interface normal jump conditions. We contend that a projection method (i.e.
84 this paper and [67, 68, 36]) is the more appropriate (albeit slower) method for
85 our study rather than the Lattice Boltzmann method. Also, in contrast to the
86 Lattice Boltzmann method, our interface “capturing” method, the CLSVOF
87 method[53, 55], maintains the gas/liquid interface as sharp, enables accurate
88 approximation of the surface tension force, and by construction the CLSVOF
89 method preserves mass and volume within a fraction of a percent. The results
90 that we present in this article (see e.g. section 3.3.2) regarding measuring the
91 tensile strength of a bubble are unique and validated with respect to comparisons

92 with previous experimental data (where available) and grid refinement studies.
93 Admittably, each simulation on the finest resolution takes over a half a year to
94 complete on a workstation because of the following unavoidable factors: (i) the
95 large density-ratio projection method requires the solution of a large sparse, ill-
96 conditioned, matrix system at each time step, (ii) the finer the mesh, the more
97 precise the measured threshold, and right at the threshold (Taylor Deformation
98 parameter $D \approx 1!$), oscillatory behaviour is observed delaying the determination
99 of breakup or not. Finally, the larger the deformation parameter D , the longer
100 one must make the computational domain (and thereby leading to larger domain
101 aspect ratio) thereby adversely effecting the condition number even more for
102 carrying our the pressure projection.

103 To highlight the mechanisms of bubble deformation and breakup in a shear
104 flow, we juxtapose the bubble results with those of a drop. We remark that
105 while the study of critical tensile strength parameters for the bubble is sparse,
106 there have been many studies for the simpler drop problem. This is because
107 the density ratio for the drop deformation case is almost one so that it is not
108 required that the continuous phase liquid be highly viscous in order to mitigate
109 buoyancy effects. For completeness, we give a brief overview of previous “tensile
110 strength” studies pertaining to drops.

111 The study of the deformation and breakup of a drop in immiscible vis-
112 cous liquids undergoing simple linear shear flow has been investigated exten-
113 sively due to its fundamental importance to emulsion processes, materials pro-
114 cessing, mixing, and reaction devices. The pioneering experimental work on
115 this problem was performed by Taylor in the early 1930s [58, 59], and the
116 subsequent theoretical and experimental progress up to the 1980s and 1990s
117 was reviewed in [38] and [50], respectively. By the 2000s, progress in com-
118 putational fluid dynamics (CFD) techniques and increased access to powerful
119 computing resources led to a surge of research focused on direct simulations
120 of this problem. In particular, detailed computational investigations of drop
121 breakup, based on a Volume-of-Fluid (VOF) method [18] were presented in
122 [29, 42, 44, 43, 25, 39, 40, 41]. Since then, the literature on computational stud-
123 ies on the deformation and breakup of a single or several drops in shear flow
124 has continued to grow [8, 20, 66, 3, 22, 9, 26, 27, 21, 17, 1, 69] and a variety
125 of numerical techniques have been developed to tackle this problem, including
126 boundary-integral approaches [7, 23], lattice Boltzmann methods [19, 26], front
127 tracking schemes [60], and interface-capturing level set methods [54].

128 Thus, a lot of studies about the deformation and breakup of a drop in sim-
129 ple linear shear have been presented so far. In contrast, few studies have been
130 conducted on bubble deformation and breakup. In the low Capillary number,
131 high Reynolds’ number regime, there are no controlled experiments or sim-
132 ulations. We reiterate why there have been few studies regarding the “tensile
133 strength” of bubbles. Experimentally, if one wants to isolate the interplay of
134 shearing force with the bubble surface tension force, in the moderate to high
135 Reynolds number regime, and low Capillary number regime, one is restricted
136 to microgravity conditions. Computational experiments are difficult too. In
137 order to accurately compute the tensile strength of a bubble, one must resort

138 to a combination of parallel computing, the multigrid preconditioned conjugate
 139 gradient method[57, 55] for poorly conditioned large sparse matrix systems,
 140 adaptive mesh refinement[70, 55], and a robust, volume preserving interface
 141 tracking method (we use the CLSVOF method[53, 55]). These aspects of our
 142 algorithm allow one to accurately simulate the balance of the restoring bubble
 143 surface tension force against the driving wall shear force.

144 **2. Problem Description**

145 Figure 1(a) shows a schematic of the computational system for our studies
 146 of a bubble (or drop) in shear flow. The computational domain consists of a
 147 three-dimensional rectangular domain with the dimensions of L (length) $\times W$
 148 (width) $\times H$ (height). The size of L , W and H was determined after considera-
 149 tion of the sensitivity of numerical results to the domain size; numerical studies
 150 of domain-size dependence are presented in Section 3.3. All computational re-
 151 sults that follow were obtained from numerical solutions of the three-dimensional
 152 governing equations for gas-liquid/liquid-liquid flows. Computations are initial-
 153 ized with a spherical bubble (or drop) of radius $R = 5$ mm set at the center of
 154 the computational domain. The bubble (or drop) is then subjected to a linear
 155 shear flow generated by the motion of the top and bottom plates, which have
 156 constant velocity $+V$ and $-V$, respectively. In the interior of the domain, the
 157 initial velocity condition is assumed to be a simple linear profile and periodic
 158 boundary conditions are imposed along the x and y directions. Mathematically,
 159 the initial and boundary conditions are described as follows:

$$\phi(x, y, z, 0) = \sqrt{(x - \frac{L}{2})^2 + (y - \frac{W}{2})^2 + (z - \frac{H}{2})^2} - R \quad (1)$$

$$\mathbf{u}(x, y, z, 0) = \begin{pmatrix} \frac{2V}{H}(z - \frac{H}{2}) \\ 0 \\ 0 \end{pmatrix}$$

$$\phi(x + L, y, z, t) = \phi(x, y, z, t) \quad \phi(x, y + W, z, t) = \phi(x, y, z, t)$$

$$\mathbf{u}(x, y, H, t) = \begin{pmatrix} V \\ 0 \\ 0 \end{pmatrix} \quad \mathbf{u}(x, y, 0, t) = \begin{pmatrix} -V \\ 0 \\ 0 \end{pmatrix}$$

$$\mathbf{u}(x + L, y, z, t) = \mathbf{u}(x, y, z, t) \quad \mathbf{u}(x, y + W, z, t) = \mathbf{u}(x, y, z, t)$$

160 $\phi(x, y, z, t)$ is a material indicator function which is positive in the “matrix”
 161 fluid and negative in the bubble (or drop) fluid. $\mathbf{u}(x, y, z, t)$ is the velocity.

162 Common dimensionless physical parameters used to describe gas-liquid or
 163 liquid-liquid two-phase flows include the Reynolds (Re), Weber (We) (or Ca (=
 164 We/Re)) and Froude (Fr) numbers. Gas-Liquid and Liquid-Liquid two-phase
 165 flow problems are also determined by the density ratio λ and the viscosity ratio
 166 η . In the present study, in order to clearly isolate the effects of λ and η , and
 167 isolate the balance of the driving wall force with the bubble surface tension

168 force, the effect of gravity is not considered ($g = 0$) so that we ignore the effect
 169 of the Fr number $\left(= \frac{\Gamma R}{\sqrt{gR}}\right)$.

170 When comparing with previous drop studies, we fix $\lambda = 1$ for the drop cases.
 171 As a result, (for $\lambda = 1$) the following dimensionless physical parameters are used
 172 to describe the problem of drop deformation/breakup in shear flow:

$$Re = \frac{\rho_m U R}{\mu_m}, \quad Ca = \frac{\mu_m U}{\sigma}, \quad \eta = \frac{\mu_b}{\mu_m} \quad m = \text{matrix fluid} \quad (2)$$

173 U is the velocity scale and σ denotes the surface tension. For the problem of
 174 shear-induced drop deformation and breakup, the velocity is set to,

$$U = \Gamma R,$$

175 where the shear-rate is,

$$\Gamma = 2V/H.$$

176 As mentioned in the introduction, most previous drop studies set $\eta = 1$ (e.g. Li
 177 et al. [29]). Thus, for comparison with previous drop deformation and breakup
 178 problems, we set $\lambda = \eta = 1$ (and also neglect the effect of gravity so that
 179 $g = 0$). On the other hand, in our computations for bubble deformation, we
 180 set the density and viscosity of air to be $\rho_b = 1.2 \text{ kg/m}^3$ and $\mu_b = 1.8 \times 10^{-5}$
 181 Pa·s respectively. We emphasize that for consistency with previous studies (Li
 182 et al. [29], Rust and Manga [45], Müller-Fischer et al. [31], Komrakova et al.
 183 [26], Amani et al. [1]), we computationally examine the deformation and breakup
 184 of a bubble in simple linear shear flow as a function of the Re and Ca numbers.
 185 That is to say, by setting $g = 0$, we are isolating the effect of only varying Re and
 186 Ca on bubble deformation and breakup. In our controlled study, we determine
 187 the critical Re_c versus Ca curve in which Re_c corresponds to the threshold of
 188 bubble (or drop) breakup. We determine the critical Re_c versus Ca curve for
 189 strategic pairs of the density ratio and viscosity ratio.

190 In our computations, the density of the matrix fluid is fixed at $\rho_m = 1000$
 191 kg/m^3 . The surface tension at the bubble (drop) interface is $\sigma = 2.5 \times 10^{-2}$
 192 N/m. The values of Re and Ca in our simulations are controlled by changing
 193 the values of μ_m and V . Specifically, we set $\mu_m = 2.0 \times 10^{-2} \sim 6.0 \times 10^{-2}$
 194 Pa·s and $V = \text{about } 1.1 \sim 1.3 \text{ m/s}$. As a consequence, for studying bubble
 195 deformation and break-up, the density and viscosity ratios satisfy $\lambda = 1.2 \times 10^{-3}$
 196 and $\eta < 1.0 \times 10^{-3}$.

197 For readers' reference, we describe the effect of gravity here. When we apply
 198 $g = 9.8 \text{ m/s}^2$, Fr can be $Fr = 1.7 \sim 1.9$ in our computations. Although
 199 the values of Fr are not so large, the effect of gravity (inducing bubble rise
 200 motion) may not be completely negligible in terms of Fr . However, bubbles in
 201 our computations reach the breakup by way of deformation very quickly at t
 202 = about 0.5 s. Accordingly, it is expected that the effect of gravity (inducing
 203 bubble rise motion) can be small for the behavior of bubble deformation and
 204 breakup around critical Re number conditions in our study.

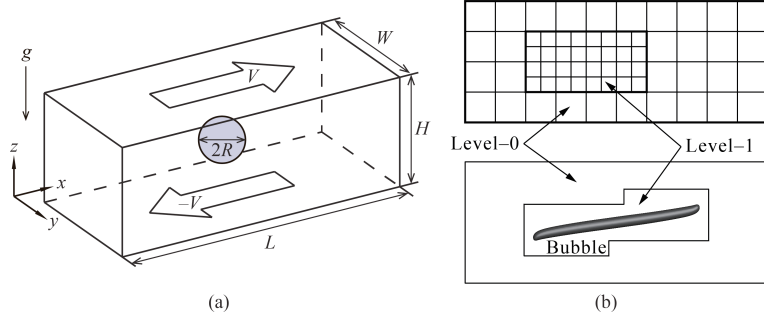


Figure 1: (a) Computational domain schematic for a bubble or drop in shear flow. Gravity is set to zero in our computations in order to isolate the effects of density and viscosity ratios. (b) (upper panel) a two-level adaptive mesh refinement (AMR) grid schematic corresponding to one of our simulations; (lower panel) snapshot of bubble deformation in simple linear shear flow.

205 3. Numerical Analysis

206 3.1. Numerical method and governing equations

207 Numerical results were obtained using the interface capturing Coupled Level
 208 Set and Volume of Fluid (CLSVOF) method (Sussman and Puckett [53], Suss-
 209 man et al. [55]), which is based on a fixed grid finite volume algorithm. The
 210 CLSVOF method is a robust numerical technique that combines some of the ad-
 211 vantages of the Volume of Fluid (VOF) method (Hirt and Nichols [18]) and the
 212 Level Set (LS) (Sussman et al. [54]) method while overcoming their weaknesses.
 213 In the VOF method, the Volume Fraction function, F , is used to represent
 214 the interface. The values of F correspond to the volume fraction of liquid in
 215 a given computational cell. In other words, $F = 0$ when a computational cell
 216 contains only gas and $F = 1$ when a computational cell contains only liquid.
 217 If $0 < F < 1$, then a computational cell contains the gas-liquid interface. The
 218 VOF method has a great advantage over the LS method in that accurate algo-
 219 rithms for advecting F can be applied so that mass/volume is conserved up to
 220 machine precision while still maintaining a sharp representation of the interface.
 221 On the other hand, the disadvantage of the VOF method in comparison to the
 222 LS method is that tangled and difficult reconstruction procedures are required
 223 for determining the slope of the piecewise linear VOF reconstructed interface.
 224 In the LS method, the signed distance function ϕ (LS function) is used to track
 225 the interface. The interface is implicitly represented by the set of points in which
 226 $\phi = 0$. Liquid and gas regions are defined as $\phi > 0$ in the liquid and $\phi < 0$ in the
 227 gas, respectively. One of the advantages of the LS method is that one can track
 228 and represent smoothly the interface, but the LS method has the disadvantage
 229 that mass/volume is not explicitly conserved. In the CLSVOF method, the cou-
 230 pling between the LS function and the VOF function occurs when computing
 231 the normal of the reconstructed interface in the VOF calculation process and
 232 also when assigning the LS function with the exact signed normal distance to
 233 the reconstructed interface in the LS calculation process. That is to say, the

piecewise linear approximation (the volume-of-fluid reconstruction step) for the VOF method is determined using the unit normal vector (\mathbf{n}) estimated from information of the LS function. By taking advantage of both methods, the evolution of the liquid-gas interface location can be computationally captured in such a way so that volume/mass is preserved to machine precision and at the same time, the interface normals and the surface tension force (which is proportional to the interface curvature) can be straightforwardly derived from the smooth level set function.

In our studies, the two-phase fluid flow is comprised of air and a viscous Newtonian liquid. The Heaviside function, $\mathcal{H}(\phi)$, which is defined as

$$\mathcal{H}(\phi) = \begin{cases} 1 & \phi \geq 0 \\ 0 & \phi < 0 \end{cases} \quad (3)$$

will be used below to distinguish each of the two fluids. A single set of three-dimensional equations governs the motion of both fluids, which are taken to be incompressible, and consists of the continuity equation and the Navier-Stokes equations with surface tension forces:

$$\nabla \cdot \mathbf{u} = 0 \quad (4)$$

$$\frac{\partial \mathbf{u}}{\partial t} + (\mathbf{u} \cdot \nabla) \mathbf{u} = \frac{1}{\rho} \nabla \cdot (-p \mathbf{I} + 2\mu \mathbf{D}) + \mathbf{g} - \frac{\sigma\kappa}{\rho} \nabla \mathcal{H} \quad (5)$$

We remark that our method is a “sharp interface method[55, 51, 24]. Thereby we do not need to specify an empirical interface thickness parameter[54, 53].

\mathbf{u} is the velocity vector, t represents time, p is the pressure, \mathbf{I} is the unit tensor, \mathbf{D} is the rate of deformation tensor ($\mathbf{D} = \frac{1}{2}(\nabla \mathbf{u} + (\nabla \mathbf{u})^T)$), ρ is the density, μ is the viscosity, κ is the interfacial curvature, and the Heaviside function $\mathcal{H}(\phi)$ is a function of the level set (LS) function ϕ . The singular Heaviside gradient term in the right hand side of equation (5) is a body force representing the surface tension force and is equivalent to specifying that the jump in the normal stress is equal to $\sigma\kappa$ (Tanguy et al. [56]). The surface tension force expressed by the singular Heaviside gradient term acts only on the gas-liquid interface. The sharp interface “Ghost Fluid Method” (Kang et al. [24]) is used to discretize the gradient of the Heaviside function as it appears in the surface tension force term. This force, upon discretization, is only non-zero across cells in which the level set function changes sign.

The interfacial curvature κ is computed with second order accuracy directly from the volume-of-fluid (VOF) function and the level set function using the height function technique (Sussman [51], Sussman et al. [55]). We remark that we get the same results if we were to compute κ directly from the LS function using the “level set” height function technique.

Since ρ and μ are taken to be constant in each fluid, with a jump at the interface, they can be expressed in terms of the Heaviside function,

$$\rho = \rho_m \mathcal{H} + \rho_b (1 - \mathcal{H}), \quad \mu = \mu_m \mathcal{H} + \mu_b (1 - \mathcal{H}). \quad (6)$$

The subscripts “b” and “m” refer to “drop or bubble” and “matrix fluid”, respectively. To represent the free surface with the CLSVOF method, we must evolve the solution to both the VOF equation for F and the LS equation for ϕ :

$$\frac{\partial F}{\partial t} + (\mathbf{u} \cdot \nabla) F = 0, \quad \frac{\partial \phi}{\partial t} + (\mathbf{u} \cdot \nabla) \phi = 0. \quad (7)$$

265 In all computations, the discretized variables p , ϕ and F are located at the
266 cell centers and the discrete velocity variable \mathbf{u} is located at cell face centers.
267 Our computations are performed using an overall second-order accurate hydro-
268 dynamic scheme. The spatial discretization uses second-order accurate, slope-
269 limited, upwind techniques for the nonlinear advective terms. The velocity and
270 pressure fields are computed using an implicit pressure projection procedure.

271 The temporal discretization of our numerical method is an operator split
272 projection method as described by Sussman et al. [55]. An outline of our method
273 is as follows (see Sussman et al. [55], section 4, for more details):

All Steps. Timestep

274 The timestep, Δt , is governed by the CFL condition and surface tension
275 (section 5.7 of Sussman et al. [55]):

$$\Delta t < \min_{i,j,k} \left(\frac{\Delta x}{2|U^n|}, \frac{1}{2} \sqrt{\frac{\rho^L}{8\pi\sigma}} \Delta x^{3/2} \right)$$

Step 1. CLSVOF interface advection

$$\begin{aligned} \phi^{n+1} &= \phi^n - \Delta t [\mathbf{u} \cdot \nabla \phi]^n \\ F^{n+1} &= F^n - \Delta t [\mathbf{u} \cdot \nabla F]^n \end{aligned}$$

Step 2. Nonlinear advective force terms

$$\mathcal{A} = [\mathbf{u} \cdot \nabla \mathbf{u}]^n$$

Step 3. Viscosity force

$$\frac{\mathbf{u}^* - \mathbf{u}^n}{\Delta t} = -\mathcal{A} + g\vec{z} - [\nabla p / \rho]^n + \frac{1}{2} \frac{\nabla \cdot (2\mu \mathbf{D}^n) + \nabla \cdot (2\mu \mathbf{D}^*)}{\rho}$$

276 Step 4. Pressure projection and ghost fluid surface tension algorithm

$$\mathbf{V} = \mathbf{u}^n + \Delta t (-\mathcal{A} + g\vec{z} + \frac{1}{2} \frac{\nabla \cdot (2\mu \mathbf{D}^n) + \nabla \cdot (2\mu \mathbf{D}^*)}{\rho})$$

277

$$\mathbf{V} = \mathbf{V} - \Delta t \frac{\sigma \kappa(\phi^{n+1})}{\rho} \nabla \mathcal{H}(\phi^{n+1})$$

278

$$\nabla \cdot \frac{\nabla p}{\rho} = \frac{1}{\Delta t} \nabla \cdot \mathbf{V}$$

279

$$\mathbf{u}^{n+1} = \mathbf{V} - \Delta t \frac{\nabla p}{\rho}$$

280 To make efficient use of computational resources, our numerical simulations
 281 utilize an adaptive hierarchy of grids based on a dynamic adaptive mesh refine-
 282 ment (AMR) technique (Sussman et al. [52]). Adaptive grids are dynamically
 283 adjusted based on the location of the deforming gas-liquid interface. In the
 284 AMR technique, the grid resolution is increased in regions near the interface
 285 while a coarser grid is used where the flow is relatively steady. The upper panel
 286 of Figure 1(b) displays a schematic view of the hierarchical grid structure and
 287 the lower panel corresponds to an actual computational example corresponding
 288 to bubble deformation in simple linear shear flow. In general, the mesh hier-
 289 archy is composed of different levels of refinement ranging from coarsest $\ell = 0$
 290 (“level-0”) to finest $\ell = \ell_{\max}$ (“level- ℓ_{\max} ”). The refinement ratio of one grid
 291 size ($\Delta x = \Delta y = \Delta z$) to the next finer level is two so that $\Delta x^{\ell+1} = 0.5\Delta x^\ell$. All
 292 computations in this study used an AMR system with a maximum prescribed
 293 level $\ell_{\max} = 1$ (as illustrated in the upper panel of Figure 1(b)). In our adaptive
 294 mesh refinement algorithm, the velocity in the coarse grid cells that neighbor
 295 fine grid cells is interpolated from the coarse grid using bilinear interpolation in
 296 order to initialize “ghost” fine cells. Thus, the bilinear interpolation procedure
 297 produces interpolated fine grid data as a linear combination of the coarse grid
 298 data.

299 3.2. Validation of the numerical method

300 The effectiveness of our sharp interface computational method has been
 301 demonstrated via grid refinement studies and comparison with experiments for
 302 the complicated rising motion of single bubbles and drops in viscous liquids
 303 Ohta and Sussman [36], Ohta et al. [32, 33, 37], Stewart et al. [49], Sussman
 304 et al. [55], the simulation of atomization in a realistic diesel injector[2], and the
 305 simulation of bubble formation due to the injection of gas through a nozzle[35].
 306 In this section, the accuracy of our computational method will be verified for
 307 the problem of shear-induced deformation of a drop and bubble. First, we com-
 308 pare quantitatively against the steady-state drop deformation results reported
 309 by Li et al. [29]. The shape of a deformed drop in simple linear shear flow is de-
 310 scribed in terms of the Taylor deformation parameter $D=(a-b)/(a+b)$, where
 311 a and b are the major and minor axes of the deformed drop respectively. For
 312 consistency, we perform numerical simulations using CLSVOF over the same
 313 computational domain and grid size used in Li et al. [29], which has dimensions
 314 $L(8R) \times W(4R) \times H(8R)$ (recall that R is the bubble/drop radius) and a level-0
 315 grid size $\Delta x = \Delta y = \Delta z = R/8$; our two-level AMR grid structure also uses a
 316 finer level-1 grid size $\Delta x^{\ell=1} = \Delta y^{\ell=1} = \Delta z^{\ell=1} = R/16$. Numerical results are

317 listed in Table 1 for D as a function of Re , with $Ca = 0.3$ and $\lambda = \eta = 1$ fixed
 318 in every case. The results in Table 1 compare computations using our CLSVOF
 319 algorithm with corresponding results that were obtained with the VOF method
 used in Li et al. [29].

Table 1: Comparison of the Taylor deformation parameter D for a drop as a function of Re ($Ca = 0.3$, $\lambda = \eta = 1$). In all cases, the domain size is $L(8R) \times W(4R) \times H(8R)$, where R is the drop radius. The CLSVOF method computations used a two-level AMR computational domain with a level-0 discretization $\Delta x^{\ell=0} = \Delta y^{\ell=0} = \Delta z^{\ell=0} = R/8$ and a level-1 discretization $\Delta x^{\ell=1} = \Delta y^{\ell=1} = \Delta z^{\ell=1} = R/16$.

Reynolds number	0.1	0.5	0.6	0.75
D (Li et al. [29])	0.3968	0.45	0.4768	Breakup
D (Our study)	0.3960	0.4570	0.4758	Breakup

320 Next, we examine the validation of our computational method in which
 321 we compare with the “bubble deformation in simple linear shear flow” results
 322 reported by Müller-Fischer et al. [31]. Müller-Fischer et al. [31] experimentally
 323 inquired into the bubble deformation under the condition of $Re \approx 0$. In our
 324 study, we computed the bubble deformation on a computational domain with
 325 dimensions $L(12R) \times W(6R) \times H(6R)$ and a computational grid in which the
 326 finest level grid size was $\Delta x^{\ell=1} = \Delta y^{\ell=1} = \Delta z^{\ell=1} = R/16$. Computations
 327 were performed for the conditions of $Ca = 0.96$ and $Ca = 1.63$ with $Re \approx 0$
 328 ($Re = 5.0 \times 10^{-4}$), $\lambda = 1.2 \times 10^{-3}$ and $\eta \leq 1.2 \times 10^{-6}$. The prescribed parameters
 329 are consistent with the experimental conditions by Müller-Fischer et al. [31].
 330 Comparisons of our numerical results and previous experimental results (Müller-
 331 Fischer et al. [31]) are tabulated in Table 2. Additionally, in Table 2, we also list
 332 experimental results with the condition of $Re \approx 0$ and $\lambda \approx \eta \approx 0$ by Rust and
 333 Manga [45]. These experimental values were obtained from the graph showing
 334 the relation of D vs Re (Rust and Manga [45]). As is clear from Table 2, our
 335 numerical results predicted larger values of D than experimental ones reported
 336 by Müller-Fischer et al. [31]. Nevertheless, our numerical results are very close to
 337 the experimental results by Rust and Manga [45], which emphasizes the intrinsic
 338 difficulties associated with experimental investigations of bubble dynamics, even
 339 in simple linear shear flow. These comparisons suggest that our computational
 340 method is effective and robust at reproducing bubble dynamics in simple linear
 341 shear flow.

342 Finally, we present a comparison with numerical results for drop breakup
 343 reported in Renardy and Cristini [44]. Figure 2 demonstrates drop breakup with
 344 pinch-off behavior for three Re and Ca conditions and with constant values of
 345 $\lambda = \eta = 1$ for all cases. The three cases that we consider correspond to (a)
 346 $Re = 10$, $Ca = 0.16$, (b) $Re = 12$, $Ca = 0.1753$, and (c) $Re = 15$, $Ca =$
 347 0.196 , and which are illustrated in Figures 2(a)-(c), respectively. The results
 348 reported in Renardy and Cristini [44], which were obtained with a VOF method,
 349 are shown inside boxes while results obtained with our CLSVOF approach are
 350 displayed outside boxes. In the computations presented in Renardy and Cristini

Table 2: Comparison of D for a bubble as a function of Ca ($Re \approx 0$, $\lambda \approx \eta \approx 0$). In all cases, the domain size is $L(12R) \times W(6R) \times H(6R)$. The CLSVOF computations used a two-level AMR computational domain with a level-0 discretization $\Delta x^{\ell=0} = \Delta y^{\ell=0} = \Delta z^{\ell=0} = R/8$ and a level-1 discretization $\Delta x^{\ell=1} = \Delta y^{\ell=1} = \Delta z^{\ell=1} = R/16$.

Capillary number	0.96	1.63
D (Müller-Fischer et al. [31])	0.37	0.58
D (Rust and Manga [45])	0.71 ± 0.05	0.81 ± 0.02
D (Our study $\Delta x^{\ell=1} = R/16$)	0.63	0.71

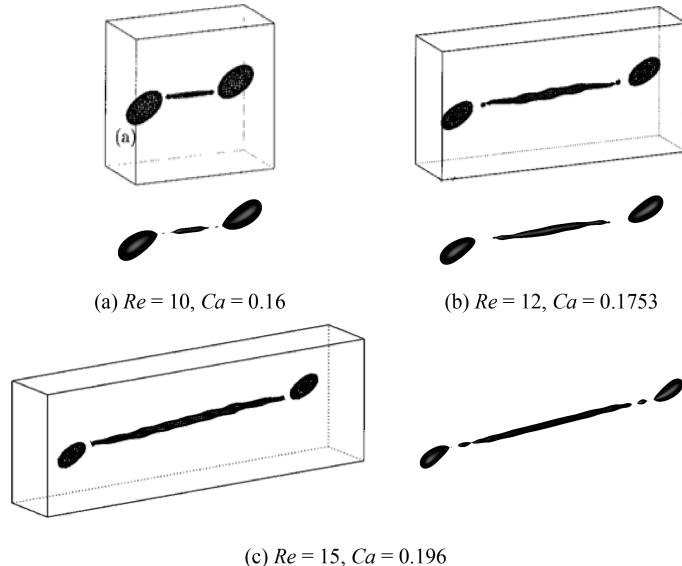


Figure 2: Comparison with results reported in Renardy and Cristini [44] (shown in bounding boxes) for drop breakup in shear flow. In Renardy and Cristini [44], the computational domain dimensions were $W = 4R$, $H = 8R$, and L was varied depending on the Re and Ca conditions. The grid size in Renardy and Cristini [44] was set to $\Delta x = \Delta y = \Delta z = R/8$. Reprinted with permission from reference Renardy and Cristini [44]. Copyright 2001, AIP Publishing. The results obtained with our CLSVOF algorithm, corresponding to each case in reference Renardy and Cristini [44], are shown without the bounding boxes. The CLSVOF method used a two-level AMR computational domain with a level-0 discretization $\Delta x^{\ell=0} = \Delta y^{\ell=0} = \Delta z^{\ell=0} = R/8$ and a level-1 discretization $\Delta x^{\ell=1} = \Delta y^{\ell=1} = \Delta z^{\ell=1} = R/16$. The onset of drop breakup is demonstrated for (a) $Re = 10$, $Ca = 0.16$, (b) $Re = 12$, $Ca = 0.1753$, and (c) $Re = 15$, $Ca = 0.196$. For all three Re and Ca conditions, $\lambda = \eta = 1$.

[44], the dimensions $W = 4R$ and $H = 8R$ were fixed, while L was changed depending on Re and Ca conditions, and the grid size was set to $\Delta x = \Delta y = \Delta z = R/8$. To compare with their results, we performed simulations with the CLSVOF method over a two-level AMR computational domain of the same dimensions and the same level-0 discretization: $\Delta x^{\ell=0} = \Delta y^{\ell=0} = \Delta z^{\ell=0} = R/8$; we set the finer level-1 grid size $\Delta x^{\ell=1} = \Delta y^{\ell=1} = \Delta z^{\ell=1} = R/16$. The

358 results shown in Figure 2 verify that our numerical approach can reproduce
 359 the same drop breakup behavior presented in Renardy and Cristini [44]. Slight
 360 differences between the results can be attributed to the increased resolution used
 361 in our study in the level-1 grid around the elongated drop.

362 The numerical validation studies performed in this section and the follow-
 363 ing section demonstrate that our numerical method can reliably determine the
 364 transition regions at which shear-induced bubble or drop deformation leads to
 365 breakup. We remark that in the next section, we demonstrate that we can
 366 expect an error of 3% for predicting the transition to break-up. The analysis
 367 in this section and the following also demonstrate that the error is reduced by
 368 a factor of 2 each time the grid is refined by a factor of 2. Also, we refer the
 369 reader to Ohta et al. [35] in which we apply our CLSVOF method for bubble
 370 formation problems.

371 *3.3. Consideration of domain and grid sizes*

372 *3.3.1. Selecting the appropriate domain size*

373 The computational domain size used in numerical studies can affect the
 374 behavior of drop deformation and breakup. Referring to Figure 1(a), with an
 375 appropriately large domain length L and a fixed width $W = 4R$, the effect of
 376 the height H on drop behavior was examined in Li et al. [29] for Stokes flows
 377 and various Ca conditions and in Komrakova et al. [26] for $Re = 1$ and $Ca =$
 378 0.27. Other related studies investigated drop breakup sensitivity (Renardy and
 379 Cristini [42]) and drop deformation sensitivity (Renardy et al. [43]) with respect
 to the entire domain size.

Table 3: Comparison of the Taylor deformation parameter D for a drop as a function of domain size ($Re = 0.75$, $Ca = 0.3$, $\lambda = \eta = 1$). CLSVOF method computations used a two-level AMR computational domain with a level-0 discretization $\Delta x^{\ell=0} = \Delta y^{\ell=0} = \Delta z^{\ell=0} = R/8$ and a level-1 discretization $\Delta x^{\ell=1} = \Delta y^{\ell=1} = \Delta z^{\ell=1} = R/16$.

System	Domain size ($L \times W \times H$)	D
System 1	$8R \times 4R \times 8R$	Breakup
System 2	$12R \times 4R \times 8R$	Breakup
System 3	$8R \times 4R \times 6R$	0.541
System 4	$8R \times 6R \times 6R$	0.466
System 5	$8R \times 8R \times 8R$	0.460
System 6	$8R \times 16R \times 16R$	0.460

380 Here we investigate the drop dynamics sensitivity to domain size around
 381 the critical Reynolds number $Re_c = 0.75$. Specifically, we consider domain size
 382 sensitivity for the condition of $Re = 0.75$, $Ca = 0.3$, and $\lambda = \eta = 1$, which is a
 383 condition used in the comparison studies of the previous section. As shown in
 384 Table 1, the drop breaks up for the condition of $Re = 0.75$ and $Ca = 0.3$ with
 385 a domain size of $L(8R) \times W(4R) \times H(8R)$. Results for domain size sensitivity
 386 for six domain systems, all of which use a level-1 grid size $\Delta x^{\ell=1} = \Delta y^{\ell=1} =$
 387

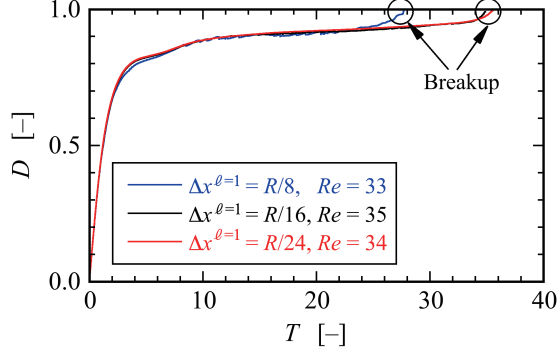


Figure 3: Time evolution of the deformation parameter D versus dimensionless time $T = \Gamma t$ for a bubble, obtained with three grid systems at different resolutions. All three resolutions use a two-level AMR grid with an effective fine resolution grid size $\Delta x^{\ell=1} = \Delta y^{\ell=1} = \Delta z^{\ell=1}$. The evolution of D using the first system, where $\Delta x^{\ell=1} = R/8$, is shown in blue and it predicts that bubble breakup occurs at a Reynolds number $Re = 33$. The evolution of D using the second system, where $\Delta x^{\ell=1} = R/16$, is shown in black and it predicts that bubble breakup occurs at a Reynolds number $Re = 35$. Results with the third system, shown in red, use $\Delta x^{\ell=1} = R/24$, and they predict that breakup occurs at $Re = 34$. The capillary number corresponding to these results is $Ca = 1.0$. ($\lambda = 1.2 \times 10^{-3}$, $\eta < 1.0 \times 10^{-3}$)

³⁸⁸ $\Delta z^{\ell=1} = R/16$, are tabulated in Table 3. Note that the domain size used in the
³⁸⁹ comparison study (Table 1) corresponds to System 1.

³⁹⁰ The results in Table 3 suggest that drop deformation is promoted when we
³⁹¹ use a domain size with $W = 4R$. In contrast, the drop does not break up and
³⁹² becomes stable with a deformed shape if we set L large enough and $W \geq 6R$ and
³⁹³ $H \geq 6R$. Since the value of D for the domain size $L(8R) \times W(6R) \times H(6R)$ differs
³⁹⁴ by only 1.3% with the value for the domain size of $L(8R) \times W(16R) \times H(16R)$,
³⁹⁵ in the results that follow we set the width to $W = 6R$ and the height to $H = 6R$
³⁹⁶ to minimize the number of computational grid nodes along those directions. To
³⁹⁷ determine the critical Reynolds number Re_c (with $Ca = 0.3$), we consider a
³⁹⁸ domain size of $L(24R) \times W(6R) \times H(6R)$, and we find that the drop reaches a
³⁹⁹ stable state with deformation parameter $D=0.549$ for $Re = 1.0$, while a value
⁴⁰⁰ of $Re = 1.1$ leads to drop breakup.

⁴⁰¹ 3.3.2. Selecting the appropriate grid size

⁴⁰² The grid size and adaptive meshing strategy that we adopt is chosen in order
⁴⁰³ to answer the research question as to the conditions which determine whether
⁴⁰⁴ a bubble in shear flow will break-up or not. In such a case, we must accurately
⁴⁰⁵ capture the balance of forces with respect to the (non-local) force exerted from
⁴⁰⁶ the wall driven flow acting against the interfacial surface tension force. The
⁴⁰⁷ accuracy of the “Critical Reynolds Number” depends on the largest Taylor De-
⁴⁰⁸formation parameter D that is supported by the grid (see e.g. Figures 8 and
⁴⁰⁹ 11). As we report here, we have found that as long as the grid size is fine enough
⁴¹⁰ to support a Taylor Deformation parameter $D < 0.95$, then the transition re-

411 gion (i.e. “Critical Reynolds number”) (see Figures 3 and 12) will be captured
412 with a tolerance of three percent. The simulation time becomes impractical if
413 we were to try to further improve the “critical Reynolds number” accuracy. A
414 smaller tolerance would necessitate a larger supported Deformation parameter
415 D which would in turn necessitate a higher aspect ratio computational domain,
416 increased droplet surface area at break-up, increased number of time steps, and
417 higher resolution for representing the drop/bubble at its thinnest point.

418 We make the distinction between our present research, and the research
419 found in the work of Zhang et al. [67, 68] on predicting the conditions for bubble
420 mergers. Even in the most extreme cases for mergers, the largest Deformation
421 parameter never exceeds 0.4 in Zhang et al. [67]. In summary, our gridding
422 requirements necessitate grid points distributed relatively evenly throughout the
423 computational domain when a bubble is stretched to a $D = 0.9$ Deformation,
424 whereas in Zhang et al. [67] the gridding strategy necessitates a more localized
425 strategy.

426 The numerical results presented in this and the previous section used a
427 finest-level grid size set to $\Delta x^{\ell=1} (= \Delta y^{\ell=1} = \Delta z^{\ell=1}) = R/16$. To verify the
428 adequacy of this grid resolution, we present grid refinement results for a bubble
429 breakup simulation with $Ca = 1.0$, which corresponds to the most deformable
430 and stretchable bubble case considered in our numerical studies. We use three
431 different grid systems, (i) $\Delta x^{\ell=1} = R/8$, (ii) $\Delta x^{\ell=1} = R/16$, and (iii) $\Delta x^{\ell=1} =$
432 $R/24$, in order to determine Re_c . Figure 3 shows the time evolution of the
433 deformation parameter D over time for the three grid systems; the x -axis is a
434 dimensionless time defined by $T = \Gamma t$ and the y -axis is D . The results show that
435 bubble breakup occurs at $Re_c = 35$ for the grid system with $\Delta x^{\ell=1} = R/16$,
436 while the finer computational grid with $\Delta x^{\ell=1} = R/24$ predicts a critical value of
437 $Re_c = 34$. For the $\Delta x^{\ell=1} = R/8$ results, it is clear that the $R/8$ resolution is too
438 coarse in order to capture the proper break-up time, albeit the critical Reynolds’
439 number, $Re_c = 33$, was still close to the finer grid resolution cases. Note that
440 although the time evolution of D for the two finer resolution systems ($R/16$ and
441 $R/24$) is consistent between the two, (the predicted critical Reynolds numbers
442 differ by $\sim 3\%$), the computational time using the grid system with $\Delta x^{\ell=1} =$
443 $R/24$ was more than 6 times longer than the one based on the coarser system
444 with $\Delta x^{\ell=1} = R/16$. We remark that in our search for Re_c , we considered a wide
445 range of values of Ca and we found it necessary to use a large L ($\sim 24R$) since
446 for certain shear flows the bubble can stretch significantly without breaking up.
447 Nevertheless, for the conditions presented in this section, the results indicate
448 that our numerical approach, even with a finest-level resolution set to $\Delta x^{\ell=1} =$
449 $R/16$, is capable of accurately reproducing bubble deformation and breakup
450 without sacrificing any essential dynamical features.

451 **4. Results and Discussion**

452 *4.1. Drop deformation and breakup*

453 To illustrate the differences in deformation and breakup between a drop
454 and a bubble around critical conditions, we first present numerical results for

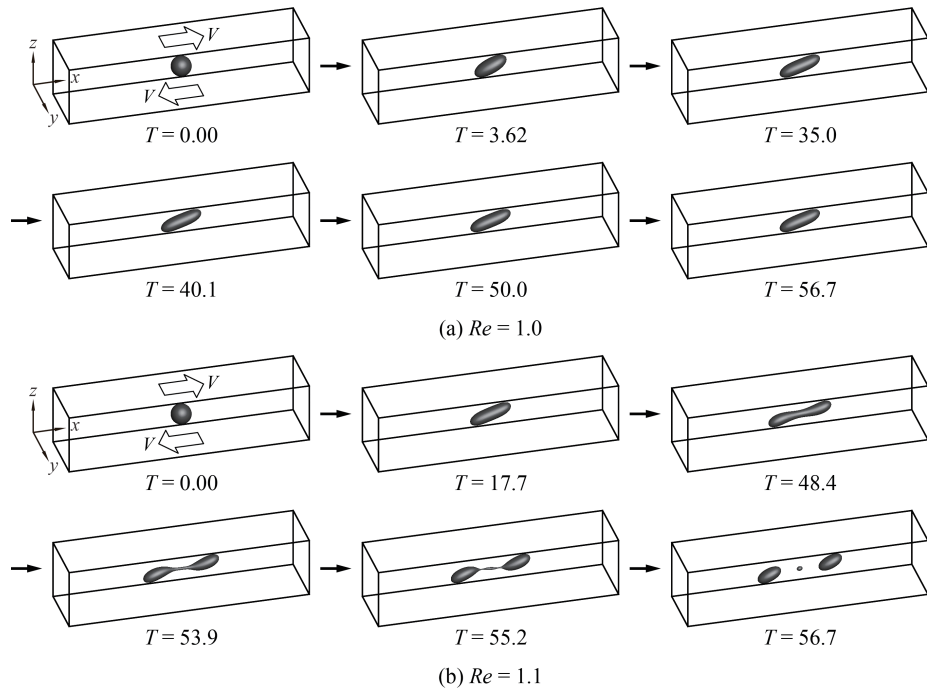


Figure 4: Time evolution of drop deformation and breakup in shear flow at the condition of $Ca = 0.3$ with (a) $Re = 1.0$ and (b) $Re = 1.1$. The “drop” critical Reynolds number corresponding to $Ca = 0.3$ is $1.0 < Re_c < 1.1$. ($\lambda = \eta = 1.0$)

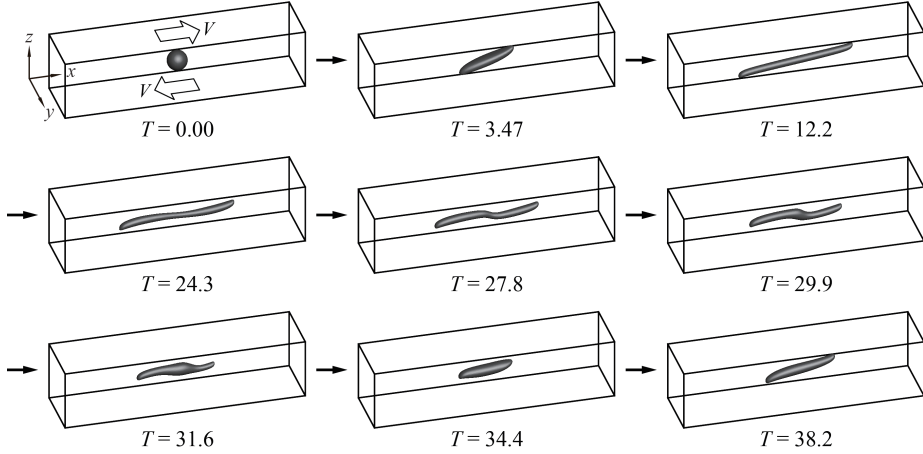


Figure 5: Time evolution of bubble deformation in shear flow at the condition of $Ca = 0.3$ and $Re = 92$. The “bubble” critical Reynolds number corresponding to $Ca = 0.3$ is $92 < Re_c < 93$. In contrast to the drop deformation case, when Re is slightly below Re_c (See Figure 4.1 $Re = 1.0$ for the drop case), the bubble shape will not reach a steady shape, instead the bubble shape alternates between the shapes “slightly stretched” ($T = 3.47$), fully stretched and “doglegged” ($T = 27.8$) and “almost” back to the original “slightly stretched” case ($T = 34.4$). ($\lambda = 1.2 \times 10^{-3}$, $\eta < 1.0 \times 10^{-3}$)

455 drop deformation. The time evolution of drop deformation and breakup in
 456 simple linear shear flow for two conditions is shown in Figure 4; the first case,
 457 shown in Figure 4(a), uses $Ca = 0.3$ and $Re = 1.0$, while the second case,
 458 depicted in Figure 4(b), uses $Ca = 0.3$ and $Re = 1.1$. Using a domain size of
 459 $L(24R) \times W(6R) \times H(6R)$, in the case with $Re = 1.0$, the drop gradually deforms
 460 and finally attains a stable deformed state. After $T = 35.0$, the drop remains a
 461 **stable deformed state with $D = 0.549$** . Over the same domain, for the case with
 462 $Re = 1.1$, the “mother” drop elongates over time and the volume at the ends
 463 of the deforming drop expands; that is, both ends of the drop become bulb-
 464 shaped. As time progresses, particularly over the time interval $48.4 \leq T \leq 55.2$,
 465 a thread-bridge forms between the bulbous ends and the thread-bridge becomes
 466 thinner. Finally, at around the dimensionless time $T \sim 56.7$, the mother drop
 467 breaks up, forming two “daughter” drops through the pinch off; one satellite
 468 drop is also generated between the pinched off daughter drops.

469 4.2. Bubble deformation and breakup

470 Next we present numerical results that illustrate the conditions that lead
 471 to bubble deformation without breakup as well as conditions where the bubble
 472 deforms and ultimately breaks up. The time evolution of shear-induced bubble
 473 deformation without breakup at the condition of $Ca = 0.3$ and $Re = 92$ is
 474 depicted in Figure 5 and the bubble breakup process with flow condition of
 475 $Ca = 0.3$ and $Re = 93$ is illustrated in Figure 6. The results indicate that
 476 the critical Reynolds number is approximately $Re_c = 93$ (with $Ca = 0.3$).

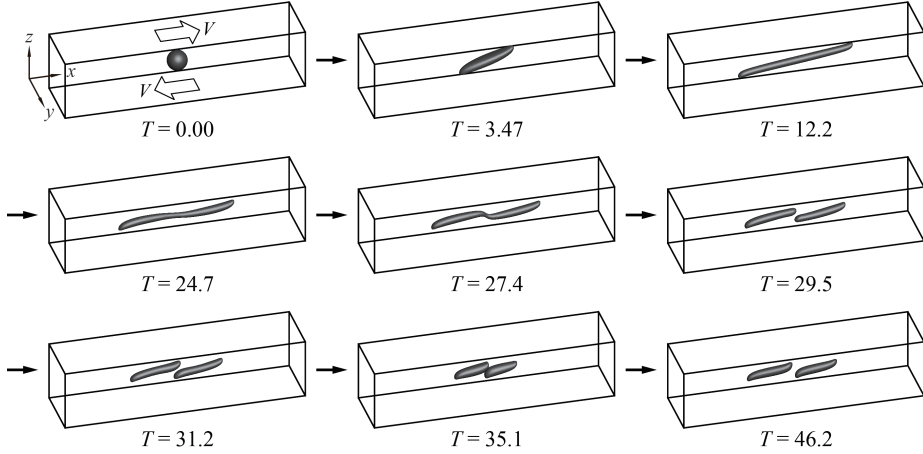


Figure 6: Time evolution of bubble deformation in shear flow at the condition of $Ca = 0.3$ and $Re = 93$. The “bubble” critical Reynolds number corresponding to $Ca = 0.3$ is $92 < Re_c < 93$. ($\lambda = 1.2 \times 10^{-3}$, $\eta < 1.0 \times 10^{-3}$)

477 A comparison with the drop breakup dynamics presented in Section 4.1 and
 478 the corresponding processes for bubble deformation and breakup exhibit very
 479 distinct features. First, we note that a relatively large shear force magnitude is
 480 required for bubble breakup ($\lambda = 1.2 \times 10^{-3}$, $\eta < 1.0 \times 10^{-3}$) compared with the
 481 case of the drop ($\lambda = \eta = 1$). Then, for the same value of $Ca = 0.3$, the critical
 482 Reynolds number for the bubble is around 85 times larger than that for the
 483 drop. Focusing on the bubble dynamics with no-breakup (Figure 5), the results
 484 show that the bubble is largely elongated in the x -direction at the early stages
 485 ($T \leq 24.3$) of bubble deformation, but the bubble does not develop the bulb-
 486 like shape (large volume areas) at both ends present in the drop deformation
 487 process. It is also evident that the ends of the deforming bubble develop cusped
 488 shapes under the influence of the strong shear flow. **In providing a more detailed**
 489 **description, very large shear forces are required to deform the bubble because**
 490 **$\lambda \simeq 0$ and $\eta \simeq 0$.** Thus, the bubble undergoing large shear forces at $T > 0$
 491 is largely stretched long the shear flow direction, and the very long elongated
 492 bubble with cusped shapes is formed. Accordingly, the bubble finally breaks up
 493 through f the elongated shape without forming a bulb-like shape. A noteworthy
 494 feature for the non-breaking bubble is that it does not settle into a deformed
 495 stable state as in the case of drop deformation presented in Figure 4.1(a). After
 496 an initial elongation process, the bubble enters a shrinking phase ($T = 27.8$)
 497 where the doglegged shape formed at the center of the bubble returns to a
 498 smaller deformed shape ($T = 34.4$) that is similar to its earlier shape ($T = 34.7$).
 499 However, when we compare the early deformed bubble shape at $T = 34.7$ with
 500 the shape at $T = 34.4$, it is clear that the shapes are not identical. Following the
 501 shrinking phase, the bubble begins to stretch again ($T = 38.2$) and the bubble
 502 oscillates between its elongated shape and shortened geometry.

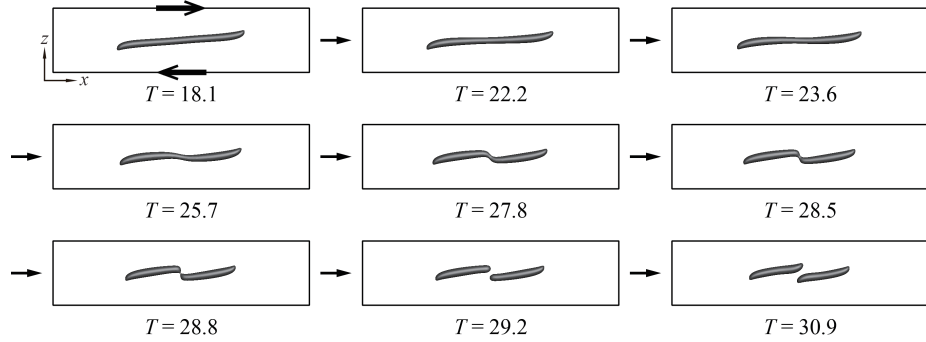


Figure 7: Detail of bubble breakup process in shear flow at the condition of $Ca = 0.3$ and $Re = 93$. The “bubble” critical Reynolds number corresponding to $Ca = 0.3$ is $92 < Re_c < 93$. ($\lambda = 1.2 \times 10^{-3}$, $\eta < 1.0 \times 10^{-3}$)

For the case of bubble breakup (Figure 6), we observe that the deformation process is almost the same as the no-breakup case until the doglegged shape is formed at $T \sim 27.4$. The bubble finally breaks during the time interval $27.7 \leq T \leq 29.5$. For a closer examination of the bubble breakup process, a detailed panel of cross-sectional slices in the xz -plane through the bubble shape center is presented in Figure 7. The images displayed in Figure 7, which are taken at shorter time intervals than those shown in Fig. 6, reveal that the bubble breaks up into two daughter bubbles due to the pinch off at the thread-bridge part of the doglegged shape during the shrinking process ($T = 28.5 \sim 28.8$). After breaking up, the two daughter bubbles migrate to the center: the left daughter bubble moves toward the right-side of the domain and the right daughter bubble moves to the left side (see results for $T = 29.5 \sim 35.1$ in Figure 6 and for $T = 28.8 \sim 30.9$ in Figure 7). The two daughter bubbles then momentarily congregate near the domain center ($T = 35.1$ in Figure 6), before they slowly start to separate: the left daughter bubble moves to the left and the right daughter bubble moves to the right ($T = 46.2$ in Figure 6). The results clearly demonstrate that the bubble breakup process is markedly different from the analogous drop breakup process with $\lambda = 1$ and $\eta = 1$. Note that the appearance of deformation and breakup of the drop will largely depend on the viscosity ratios.

4.3. Shear stress acting on the bubble

In the previous section, the appearance of bubble deformation and breakup was discussed. It is expected that a large deformation and breakup of the bubble are closely related to the state of shear stress acting on the bubble. Figure 8 shows the shear stress profile around a bubble for two Reynolds numbers under the condition of $Ca = 0.3$: Reynolds number equal to 50 and 93. The shear stress profile on the left corresponds to the case of $Re = 50$ and the right side shows the shear stress profile for the case of $Re = 93$. The normalized shear stress, $\tau^* = \tau/\tau_0$, is defined as a ratio of the local shear stress $\tau = \mu_m \sqrt{2\mathbf{D} : \mathbf{D}}$

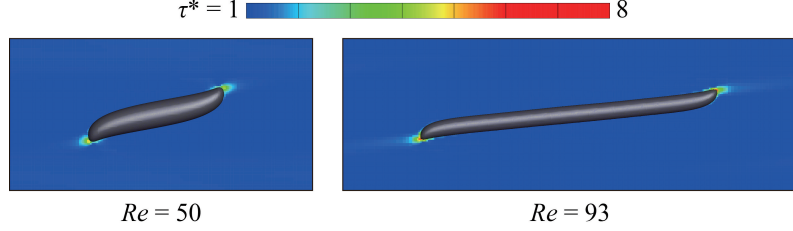


Figure 8: Normalized shear stress τ^* around a bubble for two Reynolds numbers under the condition of $Ca = 0.3$. The left image shows the shear stress profile at $Re = 50$ and the right image at $Re = 93$.

and the apparent shear stress $\tau_0 = \mu_m \Gamma$. In this study, for a given Ca condition, the same value of τ_0 is used regardless of Re . For the case of $Re = 50$, the bubble reached a deformed stable state, **and the shear stress profile around the bubble was drawn after the bubble attained a stable deformed state.** As observed in previous sections, when the value of Re is slightly below the critical Re condition, the bubble does not settle into a deformed stable state but instead alternates in an elongation and contraction process. **The shear stress profile for the case of $Re = 93$ was depicted when the bubble sufficiently elongated ($T = 14.9$).** In comparison to the $Re = 50$ case on the left, the right image in Fig. 8 ($Re = 93$) shows a higher shear stress profile near the bubble endpoints as it undergoes an elongation state in the process toward breakup. The value of the maximum shear stress for the case of $Re = 50$ is $\tau^* \approx 6$ and the maximum shear stress for the case of $Re = 93$ at the moment shown in Fig. 8 has the value of $\tau^* \approx 8$. The shear stress profile in Fig. 8 (color contour) is drawn in the range from $\tau^* = 1$ to $\tau^* = 8$, but, for emphasis, shear stress regions with $\tau^* \geq 6$ are illustrated in red. As can be seen in the figure, the strongest shear stresses are concentrated on the ends of the bubble for both Re conditions. This indicates that the strong shear stresses acting on the ends of the bubble are responsible for much of the bubble stretching. It is important to note that the magnitude of the shear stress acting on the ends of the bubble for the case of $Re = 93$ is much larger than that for the case of $Re = 50$.

We also observe that the shear stress inside the bubble was very small relative to that of the matrix fluid due to very small density and viscosity of the bubble. Since the force of strong shear stresses acting on the ends of the bubble is difficult to transfer across the interface, as a consequence, a sufficiently large Re condition is required for large bubble deformations.

In summary, what we discover is that for the Reynolds number sufficiently below the critical value, a relatively quick unsteady elongation period gives way to a steady state (with no break up). On the other hand for Reynolds number close to the critical Reynolds number, there is a prolonged, unsteady, elongation period, in which periodic motion is observed and the deformation parameter D is close to one. The “vacillating” behavior cannot last forever, ultimately (perhaps stochastically!), the bubble will either settle down or break. We assert

565 that regardless of the outcome, this vacillating behaviour will always occur in
 566 close proximity to the critical Reynolds' number. In other words, regardless of
 567 the outcome, we claim, using the grid resolution of $R/16$, that one is assured
 568 of being within 3 percent of the critical Reynolds number (see Figure 3). In
 569 fact, we hypothesize that there will always be “vacillating” behavior if one is
 570 sufficiently close to the critical Reynolds number. i.e. given an almost infinite
 571 supply of computational resources, as one hones in closer and closer to the
 572 critical Reynolds number, a “tug of war” will be observed between the surface
 573 tension force trying to pull the bubble together versus the wall driven shear
 574 stress trying to pull the bubble apart.

575 *4.4. Velocity field outside and inside the breaking bubble*

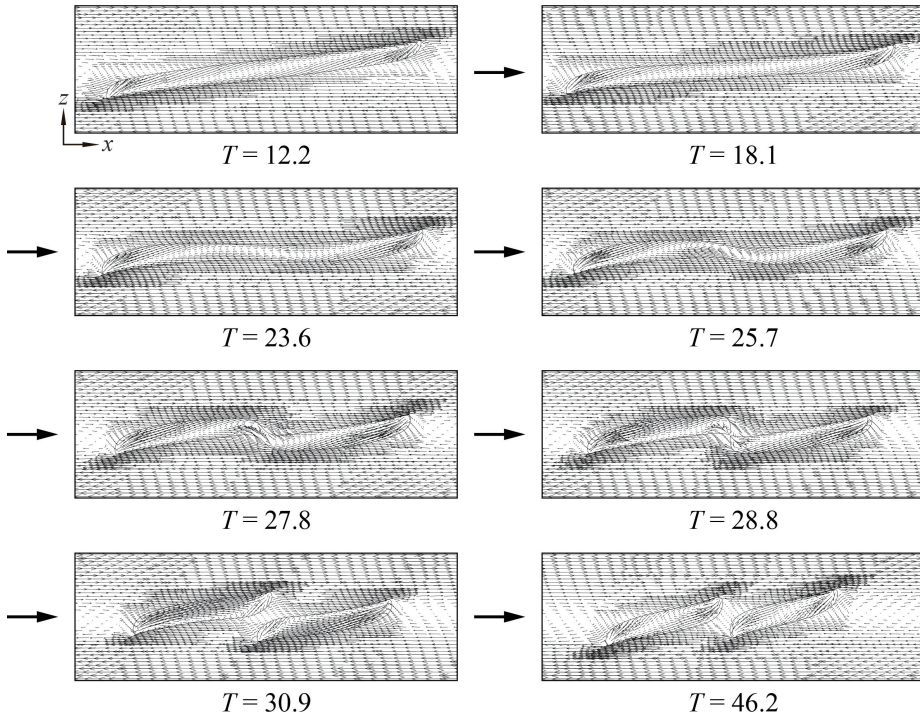


Figure 9: Fluid velocity field outside and inside the breaking bubble in shear flow at the condition $Ca = 0.3$ and $Re = 93$. The “bubble” critical Reynolds number corresponding to $Ca = 0.3$ is $92 < Re_c < 93$. ($\lambda = 1.2 \times 10^{-3}$, $\eta < 1.0 \times 10^{-3}$)

576 In this section, we consider the fluid flow velocity field outside and inside the
 577 bubble during the shear-induced breakup process. Detailed velocity fields of the
 578 deforming and breaking drop have already been presented in some references
 579 (Li et al. [29], Renardy and Cristini [42]). The velocity fields for the drop and
 580 the bubble will be influenced by the behavior of the breakup process, so the
 581 velocity fields for the drop and the bubble are not similar. Figure 9 shows the

582 velocity fields outside and inside the bubble at cross-sectional slices in the xz -
 583 plane for a flow condition of $Ca = 0.3$ and $Re = 93$. Regions around the bubble
 584 where there is a higher density of velocity vectors correspond to the level-1 grid
 585 portion of the AMR structure. The simulation results show that the velocity
 586 field inside the bubble is particularly distinct from the surrounding flow field
 587 in the exterior of the bubble. The cross-sections at $T = 12.2$ and $T = 18.1$,
 588 taken during the elongation phase, show how shear forces at the lower and
 589 upper halves of the bubble act along the bottom and top surfaces, respectively,
 590 to deform the interface. Near the left and right edges of the bubble, inward
 591 interior flows (that point toward the bubble center) begin to develop. Strong
 592 shearing forces in the exterior near the bottom-left-end and top-right-end of
 593 the bubble interact with the interior flow field through the boundary to create
 594 cusped shapes at the bottom-left and top-right ends of the bubble while the
 595 interface is laterally elongated in the x -direction. During the shrinking process,
 596 which occurs for $23.6 \leq T \leq 27.8$, inward flows within the bubble extend over
 597 a wider region and are no longer localized near the bubble edges. Then, we
 598 observe that circulating flows form at the thread-bridge part of the doglegged
 599 bubble shape over the time interval [25.7, 27.8]. During the breakup process
 600 ($T \sim 28.8$), higher-intensity inward flows are formed inside the bubble, near the
 601 pinch off region, that are naturally larger than the surrounding interior flows
 602 and which are inextricably associated with the bubble migration illustrated in
 603 Figs. 6 and 7. As time proceeds further ($T = 46.2$), distinct inward flows are
 604 formed inside the daughter bubbles; the bubbles then begin their migration
 605 toward the side walls. Considering the left daughter bubble, for example, we
 606 see that the mechanism responsible for this movement results from larger shear
 607 forces acting on the bottom-left end than those in the top-left end.

608 4.5. Effect of surface tension on bubble deformation and breakup

609 In previous sections, we considered numerical simulations of bubble defor-
 610 mation and breakup with a capillary number $Ca = 0.3$. Here, we examine
 611 similar bubble dynamics with $Ca = 0.8$ and we also investigate the effect of in-
 612 terfacial tension on bubble deformation and breakup. Using $Ca = 0.8$ for both
 613 cases, Figures 10 and 11 present the time evolution of shear-induced bubble
 614 deformation and breakup with $Re = 42$ and $Re = 43$, respectively. We note
 615 that the bubble critical Reynolds number is around $Re_c \approx 43$, whereas $Re_c \approx 0$
 616 for the corresponding case of the drop with $\lambda = \eta = 1$ (see e.g. Li et al. [29]).
 617 Note that Re_c for $Ca = 0.8$ is smaller than that for the condition of $Ca = 0.3$
 618 since the bubble at $Ca = 0.8$ is more elastic due to the weaker effect of sur-
 619 face tension in this case. The results shown in Figs. 10 and 11 indicate that
 620 the bubble deformation and breakup process for the condition of $Ca = 0.8$ is
 621 analogous to that for $Ca = 0.3$. For the case of bubble deformation without
 622 breakup (Fig. 10), the bubble initially assumes a long elongated shape along the
 623 x -direction at around $T = 17.0$. The bubble then enters a compression stage
 624 over the time interval [31.3, 41.2] and subsequently starts to elongate again at
 625 $T = 45.8$. On the other hand, for the case of bubble breakup (Fig. 11), an
 626 initial elongation phase is followed by a doglegged shape formation at $T = 33.7$.

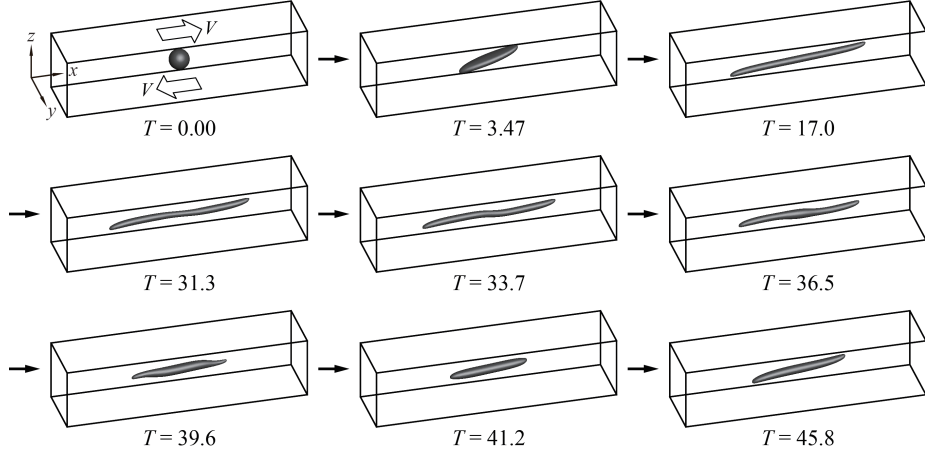


Figure 10: Time evolution of bubble deformation in shear flow at the condition of $Ca = 0.8$ and $Re = 42$. The “bubble” critical Reynolds number corresponding to $Ca = 0.8$ is $42 < Re_c < 43$. ($\lambda = 1.2 \times 10^{-3}$, $\eta < 1.0 \times 10^{-3}$)

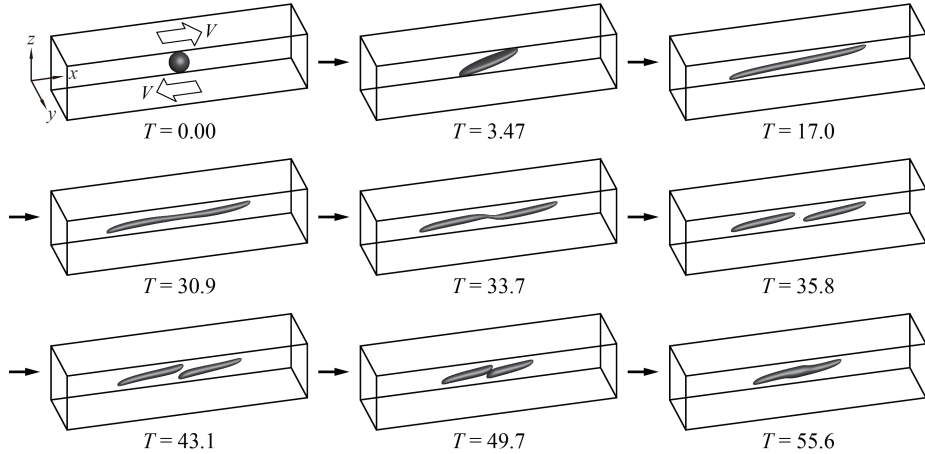


Figure 11: Time evolution of bubble deformation in shear flow at the condition of $Ca = 0.8$ and $Re = 43$. The “bubble” critical Reynolds number corresponding to $Ca = 0.8$ is $42 < Re_c < 43$. ($\lambda = 1.2 \times 10^{-3}$, $\eta < 1.0 \times 10^{-3}$)

627 After that, the bubble ruptures from the thread-bridge part of the doglegged
 628 shape and two daughter bubbles are produced ($T = 35.8$). The two daughter
 629 bubbles formed after breakup move to the central area ($T = 49.7$) as in the case
 630 of $Ca = 0.8$ and $Re = 93$, but the two bubbles eventually coalesce in a region
 631 approximately centered in the computational domain ($T = 55.6$). We note that
 632 in a real experimental setting, bubbles may coalesce after breaking up due to
 633 slight deviations of flow conditions and states. Although the process of bubble
 634 deformation and breakup for flow conditions with $Ca = 0.3$ and $Ca = 0.8$ are
 635 similar, a pronounced difference is that the bubble for $Ca = 0.8$ is more elon-
 636 gated and slender than that for $Ca = 0.3$ due to the smaller effect of surface
 637 tension for $Ca = 0.8$.

638 Table 4 lists, for representative Ca values, the corresponding critical Reynolds
 639 number, Re_c , for shear-induced bubble breakup. The data in Table 4 corre-
 640 sponds to $\lambda = 1.2 \times 10^{-3}$, $\eta < 1.0 \times 10^{-3}$, $0.3 < Ca < 1$, and the initial/boundary
 641 conditions are given by (1). The results in Table 4 indicate that sufficiently large
 642 shear forces are required for bubble breakup even for large capillary numbers.
 643 In Figure 12 we plot the smooth interpolant of the data given in Table 4 and
 644 make the hypothesis that given a new data point, (Ca, Re) , shear induced bub-
 645 ble break up will occur if the point (Ca, Re) is above the given critical curve,
 646 and the bubble will not break if the (Ca, Re) pair is below the critical curve.
 647 For comparison, a critical curve for the drop with $\lambda = \eta = 1$ is also indicated
 648 in Fig. 12. The inclusion of breakup and no-breakup critical curves, for both
 649 the drop and the bubble, will facilitate future identification of Re_c numbers—
 650 and thus a more complete general critical curve—for a wide range of high Ca
 651 numbers.

Table 4: Shear-induced bubble breakup for various flow conditions described in terms of column pairs of critical Reynolds numbers and corresponding capillary numbers. ($\lambda = 1.2 \times 10^{-3}$, $\eta < 1.0 \times 10^{-3}$)

Capillary number Ca	0.3	0.5	0.8	1.0
Critical Reynolds number Re_c	93	67	43	35

652 5. Conclusions

653 The bubble deformation and breakup process in simple linear shear flow
 654 liquid was explored numerically using the CLSVOF computational method. In
 655 this study, the critical Reynolds number Re_c , at which bubble breakup first
 656 occurs, was determined for several flow conditions, and the differences between
 657 bubble deformation and breakup were compared with the well-known analogous
 658 process of drop deformation and breakup.

659 Numerical results revealed significant differences between bubble deforma-
 660 tion and breakup and the corresponding drop dynamics. For case of bubble,
 661 it was discovered that much stronger shear flows are necessary to induce in-
 662 terface breakup compared with a drop immersed in a similar flow field. That

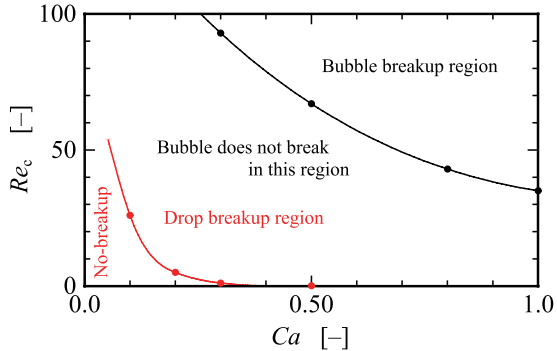


Figure 12: A plot of the critical Reynolds number versus capillary number for the data listed in Table 4. $\lambda = 1.2 \times 10^{-3}$, $\eta < 1.0 \times 10^{-3}$, $0.3 < Ca < 1$, and the initial/boundary conditions are given by (1). Given a new data point, (Ca, Re) , one can reliably predict whether the given (Ca, Re) pair will result in shear induced bubble break-up or not. Note, for the “Drop delineation curve,” $\lambda = \eta = 1$.

is, a much larger Reynolds number flow is required in order to induce bubble breakup. The behavior of bubble breakup was very similar through the Ca number range considered in our computations: the bubble underwent a similar breakup mechanism in which rupture occurred at a thread-bridge part that followed a doglegged shape formation stage. In bubble deformation without breakup, near Re_c , the bubble did not maintain a stable deformed shape, in contrast to drop deformation near the critical Reynolds number. The bubble exhibited pronounced underdamped behavior: the bubble oscillated between elongating and shrinking motions for non-rupturing flow conditions. **At the same time, bubble deformation under smaller Re conditions ($< Re_c$) becomes in a stable state.** We attribute the large differences in morphology for the bubble undergoing breakup, compared with the drop, to the density and viscosity ratio. The density and viscosity ratio remarkably impacts on bubble/drop deformation and breakup. The bubble deformation and breakup is subject to a synergistic coupling of the density and viscosity ratio, and whose effect will be examined separately in future work.

References

- [1] Amani, A., Balcázar, N., Castro, J., Oliva, A., 2019. Numerical study of droplet deformation in shear flow using a conservative level-set method. *Chemical Engineering Science* 207, 153–171. URL: <http://www.sciencedirect.com/science/article/pii/S0009250919305123>, doi:<https://doi.org/10.1016/j.ces.2019.06.014>.
- [2] Arienti, M., Li, X., Soteriou, M., Eckett, C., Sussman, M., Jensen, R., 2013. Coupled level-set/volume-of-fluid method for simulation of injector atomization. *Journal of propulsion and power* 29, 147–157.

- 689 [3] Bazhlekov, I.B., Anderson, P.D., Meijer, H.E., 2006. Numerical investigation
690 of the effect of insoluble surfactants on drop deformation and
691 breakup in simple shear flow. *Journal of Colloid and Interface Science* 298, 369 – 394. URL: <http://www.sciencedirect.com/science/article/pii/S0021979705012658>, doi:<http://dx.doi.org/10.1016/j.jcis.2005.12.017>.
- 695 [4] Bento, D., Rodrigues, R.O., Faustino, V., Pinho, D., Fernandes, C.S.,
696 Pereira, A.I., Garcia, V., Miranda, J.M., Lima, R., 2018. Deformation
697 of red blood cells, air bubbles, and droplets in microfluidic devices:
698 Flow visualizations and measurements. *Micromachines* 9, 151. URL:
699 <https://www.mdpi.com/2072-666X/9/4/151>, doi:10.3390/mi9040151.
- 700 [5] Canedo, E.L., Favelukis, M., Tadmor, Z., Talmon, Y., 1993.
701 An experimental study of bubble deformation in viscous liquids in simple shear flow. *AIChE Journal* 39, 553–559. URL:
702 <https://aiche.onlinelibrary.wiley.com/doi/abs/10.1002/aic.690390403>,
703 doi:<https://doi.org/10.1002/aic.690390403>,
704 arXiv:<https://aiche.onlinelibrary.wiley.com/doi/pdf/10.1002/aic.690390403>.
- 705 [6] Chu, P., Finch, J., Bournival, G., Ata, S., Hamlett, C., Pugh, R.J.,
706 2019. A review of bubble break-up. *Advances in Colloid and Interface Science* 270, 108–122. URL: <https://www.sciencedirect.com/science/article/pii/S0001868619300211>, doi:<https://doi.org/10.1016/j.cis.2019.05.010>.
- 711 [7] Cristini, V., Bławzdziewicz, J., Loewenberg, M., 2001. An adaptive
712 mesh algorithm for evolving surfaces: simulations of drop breakup
713 and coalescence. *Journal of Computational Physics* 168, 445 –
714 463. URL: <http://www.sciencedirect.com/science/article/pii/S0021999101967130>, doi:<http://dx.doi.org/10.1006/jcph.2001.6713>.
- 716 [8] Cristini, V., Guido, S., Alfani, A., Bławzdziewicz, J., Loewenberg, M.,
717 2003. Drop breakup and fragment size distribution in shear flow. *Journal of Rheology* 47, 1283–1298. URL: <http://scitation.aip.org/content/sor/journal/jor2/47/5/10.1122/1.1603240>, doi:<http://dx.doi.org/10.1122/1.1603240>.
- 721 [9] Croce, R., Griebel, M., Schweitzer, M.A., 2010. Numerical simulation of
722 bubble and droplet deformation by a level set approach with surface tension
723 in three dimensions. *International Journal for Numerical Methods in Fluids*
724 62, 963–993. URL: <http://dx.doi.org/10.1002/fld.2051>, doi:10.1002/fld.2051.
- 726 [10] Drenckhan, W., Saint-Jalmes, A., 2015. The science of foaming. *Advances in Colloid and Interface Science* 222, 228–259. URL: <https://www.sciencedirect.com/science/article/pii/S0001868615000603>,
727 doi:<https://doi.org/10.1016/j.cis.2015.04.001>. reinhard Miller,
728 Honorary Issue.

- 731 [11] Eftekhari, M., Schwarzenberger, K., Heitkam, S., Eckert, K.,
732 2021a. Interfacial flow of a surfactant-laden interface under asym-
733 metric shear flow. *Journal of Colloid and Interface Science* 599,
734 837–848. URL: <https://www.sciencedirect.com/science/article/pii/S0021979721006457>, doi:<https://doi.org/10.1016/j.jcis.2021.04.126>.
- 737 [12] Eftekhari, M., Schwarzenberger, K., Heitkam, S., Javadi, A.,
738 Bashkatov, A., Ata, S., Eckert, K., 2021b. Interfacial be-
739 havior of particle-laden bubbles under asymmetric shear flow.
740 *Langmuir* 37, 13244–13254. URL: <https://doi.org/10.1021/acs.langmuir.1c01814>,
741 doi:<https://doi.org/10.1021/acs.langmuir.1c01814>. pMID:
742 [arXiv:https://doi.org/10.1021/acs.langmuir.1c01814](https://doi.org/10.1021/acs.langmuir.1c01814).
743 34726918.
- 744 [13] Ervin, E., Tryggvason, G., 1997. The rise of bubbles in a vertical shear
745 flow. *Journal of Fluids Engineering* 119(2), 443–449.
- 746 [14] Fang, Z., Shuai, Y., Huang, Z., Wang, J., Yang, Y., 2024. Inten-
747 sification of polyethylene devolatilization in twin-screw extruder
748 with additives. *Polymer Engineering & Science* 64, 2961–2974.
749 URL: <https://4spepublications.onlinelibrary.wiley.com/doi/abs/10.1002/pen.26738>,
750 doi:<https://doi.org/10.1002/pen.26738>,
751 arXiv:<https://4spepublications.onlinelibrary.wiley.com/doi/pdf/10.1002/pen.26738>.
- 752 [15] Frense, E., Rüdiger, F., Fröhlich, J., 2024. Modeling of dynamic bub-
753 ble deformation and breakup in t-junction channel flow. *Chemical En-
754 gineering Science* 300, 120579. URL: <https://www.sciencedirect.com/science/article/pii/S0009250924008790>, doi:<https://doi.org/10.1016/j.ces.2024.120579>.
- 757 [16] Gao, S., Shi, Y., Pan, G., Quan, X., 2022. Research on the
758 effect of asymmetric bubbles on the load characteristics of projec-
759 tiles during an underwater salvo. *Applied Ocean Research* 124,
760 103212. URL: <https://www.sciencedirect.com/science/article/pii/S0141118722001535>, doi:<https://doi.org/10.1016/j.apor.2022.103212>.
- 763 [17] Hernandez, F.H., Rangel, R.H., 2017. Breakup of drops in simple
764 shear flows with high-confinement geometry. *Computers & Fluids* 146,
765 23 – 41. URL: <http://www.sciencedirect.com/science/article/pii/S0045793017300038>, doi:<https://doi.org/10.1016/j.compfluid.2017.01.001>.
- 768 [18] Hirt, C., Nichols, B., 1981. Volume of fluid (vof) method
769 for the dynamics of free boundaries. *Journal of Computational
770 Physics* 39, 201 – 225. URL: <http://www.sciencedirect.com/science/article/pii/0021999181901455>, doi:[http://dx.doi.org/10.1016/0021-9991\(81\)90145-5](http://dx.doi.org/10.1016/0021-9991(81)90145-5).

- 773 [19] Inamuro, T., 2006. Lattice boltzmann methods for viscous fluid flows and
774 for two-phase fluid flows. *Fluid Dynamics Research* 38, 641. URL: <http://stacks.iop.org/1873-7005/38/i=9/a=A04>.
- 776 [20] Inamuro, T., Tomita, R., Ogino, F., 2003. Lattice boltzmann simulations of drop deformation and breakup in simple shear flows. *International Journal of Modern Physics B* 17, 21–26. URL: <http://www.worldscientific.com/doi/abs/10.1142/S0217979203017035>, doi:10.1142/S0217979203017035.
- 781 [21] Ioannou, N., Liu, H., Zhang, Y., 2016. Droplet dynamics
782 in confinement. *Journal of Computational Science* 17, 463 –
783 474. URL: <http://www.sciencedirect.com/science/article/pii/S1877750316300308>, doi:<https://doi.org/10.1016/j.jocs.2016.03.009>. *discrete Simulation of Fluid Dynamics* 2015.
- 786 [22] Janssen, P., Anderson, P., 2008. A boundary-integral model for
787 drop deformation between two parallel plates with non-unit viscosity
788 ratio drops. *Journal of Computational Physics* 227, 8807–
789 8819. URL: <http://www.sciencedirect.com/science/article/pii/S002199910800346X>, doi:<http://dx.doi.org/10.1016/j.jcp.2008.06.027>.
- 792 [23] Janssen, P.J.A., Anderson, P.D., 2007. Boundary-integral method
793 for drop deformation between parallel plates. *Physics of Fluids*
794 19. URL: <http://scitation.aip.org/content/aip/journal/pof2/19/4/10.1063/1.2715621>, doi:<http://dx.doi.org/10.1063/1.2715621>.
- 796 [24] Kang, M., Fedkiw, R.P., Liu, X.D., 2000. A boundary condition capturing
797 method for multiphase incompressible flow. *Journal of scientific computing*
798 15, 323–360.
- 799 [25] Khismatullin, D.B., Renardy, Y., Cristini, V., 2003. Inertia-induced
800 breakup of highly viscous drops subjected to simple shear. *Physics of Fluids*
801 15, 1351–1354. doi:<http://dx.doi.org/10.1063/1.1564825>.
- 802 [26] Komrakova, A., Shardt, O., Eskin, D., Derksen, J., 2014. Lattice
803 boltzmann simulations of drop deformation and breakup in shear flow.
804 *International Journal of Multiphase Flow* 59, 24 – 43. URL: <http://www.sciencedirect.com/science/article/pii/S0301932213001547>,
805 doi:<http://dx.doi.org/10.1016/j.ijmultiphaseflow.2013.10.009>.
- 807 [27] Komrakova, A., Shardt, O., Eskin, D., Derksen, J., 2015. Effects
808 of dispersed phase viscosity on drop deformation and breakup
809 in inertial shear flow. *Chemical Engineering Science* 126, 150 –
810 159. URL: <http://www.sciencedirect.com/science/article/pii/S000925091400726X>, doi:<http://dx.doi.org/10.1016/j.ces.2014.12.012>.

- 813 [28] Legendre, D., Magnaudet, J., 1998. The lift force on a spherical bubble in
814 a viscous linear shear flow. *Journal of Fluid Mechanics* 368, 81–126.
- 815 [29] Li, J., Renardy, Y., Renardy, M., 2000. Numerical simulation of
816 breakup of a viscous drop in simple shear flow through a volume-of-fluid
817 method. *Physics of Fluids* 12, 269–282. URL: <http://scitation.aip.org/content/aip/journal/pof2/12/2/10.1063/1.870305>, doi:<http://dx.doi.org/10.1063/1.870305>.
- 820 [30] Lohse, D., 2018. Bubble puzzles: from fundamentals to applications. *Physical review fluids* 3, 110504.
- 822 [31] Müller-Fischer, N., Tobler, P., Dressler, M., Fischer, P., Windhab, E.J.,
823 2008. Single bubble deformation and breakup in simple shear flow. *Experiments in fluids* 45, 917–926.
- 825 [32] Ohta, M., Akama, Y., Yoshida, Y., Sussman, M., 2014. Influence of the
826 viscosity ratio on drop dynamics and breakup for a drop rising in an immiscible
827 low-viscosity liquid. *Journal of Fluid Mechanics* 752, 383–409.
828 doi:[10.1017/jfm.2014.339](https://doi.org/10.1017/jfm.2014.339).
- 829 [33] Ohta, M., Furukawa, T., Yoshida, Y., Sussman, M., 2019. A
830 three-dimensional numerical study on the dynamics and deformation
831 of a bubble rising in a hybrid carreau and fene-cr modeled polymeric
832 liquid. *Journal of Non-Newtonian Fluid Mechanics* 265, 66–
833 78. URL: <https://www.sciencedirect.com/science/article/pii/S0377025718301952>, doi:<https://doi.org/10.1016/j.jnnfm.2018.12.012>.
- 836 [34] Ohta, M., Imura, T., Yoshida, Y., Sussman, M., 2005. A computational
837 study of the effect of initial bubble conditions on the motion of a gas bubble
838 rising in viscous liquids. *International journal of multiphase flow* 31, 223–
839 237.
- 840 [35] Ohta, M., Kikuchi, D., Yoshida, Y., Sussman, M., 2011. Robust numerical
841 analysis of the dynamic bubble formation process in a viscous liquid.
842 *International Journal of Multiphase Flow* 37, 1059–1071.
- 843 [36] Ohta, M., Sussman, M., 2012. The buoyancy-driven motion
844 of a single skirted bubble or drop rising through
845 a viscous liquid. *Physics of Fluids* 24, 112101. URL:
846 <https://doi.org/10.1063/1.4765669>, doi:[10.1063/1.4765669](https://doi.org/10.1063/1.4765669),
847 arXiv:https://pubs.aip.org/aip/pof/article-pdf/doi/10.1063/1.4765669/14128560/112101_1.pdf
- 848 [37] Ohta, M., Yamaguchi, S., Yoshida, Y., Sussman, M., 2010. The sensitivity
849 of drop motion due to the density and viscosity ratio. *Physics of Fluids* 22,
- 850 [38] Rallison, J.M., 1984. The deformation of small viscous drops
851 and bubbles in shear flows. *Annual Review of Fluid Mechanics* 16, 45–66. URL: <http://dx.doi.org/10.1146/annurev.fl.16.240284.000255>

- 853 16.010184.000401, doi:10.1146/annurev.fl.16.010184.000401,
854 arXiv:<http://dx.doi.org/10.1146/annurev.fl.16.010184.000401>.
- 855 [39] Renardy, Y., 2006. Numerical simulation of a drop undergoing large am-
856 plitude oscillatory shear. *Rheologica acta* 45, 223–227.
- 857 [40] Renardy, Y., 2007. The effects of confinement and inertia on the production
858 of droplets. *Rheologica Acta* 46, 521–529. URL: <http://dx.doi.org/10.1007/s00397-006-0150-y>, doi:10.1007/s00397-006-0150-y.
- 860 [41] Renardy, Y., 2008. Effect of startup conditions on drop breakup under
861 shear with inertia. *International Journal of Multiphase Flow* 34, 1185 – 1189. URL: <http://www.sciencedirect.com/science/article/pii/S030193220800089X>, doi:<http://dx.doi.org/10.1016/j.ijmultiphaseflow.2008.04.004>.
- 865 [42] Renardy, Y., Cristini, V., 2001a. Effect of inertia on drop breakup under
866 shear. *Physics of Fluids* 13, 7–13. URL: <http://scitation.aip.org/content/aip/journal/pof2/13/1/10.1063/1.1331321>, doi:<http://dx.doi.org/10.1063/1.1331321>.
- 869 [43] Renardy, Y., Cristini, V., Li, J., 2002. Drop fragment distributions un-
870 der shear with inertia. *International Journal of Multiphase Flow* 28, 1125
871 – 1147. URL: <http://www.sciencedirect.com/science/article/pii/S0301932202000228>, doi:[http://dx.doi.org/10.1016/S0301-9322\(02\)00022-8](http://dx.doi.org/10.1016/S0301-9322(02)00022-8).
- 874 [44] Renardy, Y.Y., Cristini, V., 2001b. Scalings for fragments produced
875 from drop breakup in shear flow with inertia. *Physics of Fluids* 13,
876 2161–2164. URL: <https://doi.org/10.1063/1.1384469>, doi:10.1063/
877 1.1384469, arXiv:<https://doi.org/10.1063/1.1384469>.
- 878 [45] Rust, A., Manga, M., 2002. Bubble shapes and orientations in low re-
879 simple shear flow. *Journal of Colloid and Interface Science* 249, 476–
880 480. URL: <https://www.sciencedirect.com/science/article/pii/S0021979702982925>, doi:<https://doi.org/10.1006/jcis.2002.8292>.
- 882 [46] Sanogo, B., Souidi, K., Marcati, A., Vial, C., 2023. Food aeration: Ef-
883 fect of the surface-active agent type on bubble deformation and break-up
884 in a viscous newtonian fluid: From single bubble to process-scale. *Food*
885 *Research International* 165, 112478. URL: <https://www.sciencedirect.com/science/article/pii/S0963996923000236>, doi:<https://doi.org/10.1016/j.foodres.2023.112478>.
- 888 [47] Schlüter, M., Herres-Pawlis, S., Nieken, U., Tuttlies, U., Bothe, D., 2021.
889 Small-scale phenomena in reactive bubbly flows: Experiments, numerical
890 modeling, and applications. *Annual review of chemical and biomolecular
891 engineering* 12, 625–643.

- 892 [48] Sharifi, R., Varmazyar, M., Mohammadi, A., 2024. Investigating droplet and bubble deformation under shear flow using the multi-pseudo-potential scheme of lattice boltzmann method. *Advances in Applied Mathematics and Mechanics* 16, 519–548. URL: <https://global-sci.com/article/72820/investigating-droplet-and-bubble-deformation-under-shear-flow-using-the-multi-pseudo-potential-scheme-of-lattice-boltzmann-method>. doi:<https://doi.org/10.4208/aamm.OA-2021-0326>.
- 893
894
895
896
897
898
- 899 [49] Stewart, P., Lay, N., Sussman, M., Ohta, M., 2008. An improved sharp interface method for viscoelastic and viscous two-phase flows. *Journal of Scientific Computing* 35, 43–61.
- 900
901
- 902 [50] Stone, H.A., 1994. Dynamics of drop deformation and breakup in viscous fluids. *Annual Review of Fluid Mechanics* 26, 65–102. URL: <http://dx.doi.org/10.1146/annurev.fl.26.010194.000433>, doi:[10.1146/annurev.fl.26.010194.000433](https://doi.org/10.1146/annurev.fl.26.010194.000433), arXiv:<http://dx.doi.org/10.1146/annurev.fl.26.010194.000433>.
- 903
904
905
906
- 907 [51] Sussman, M., 2003. A second order coupled level set and volume-of-fluid method for computing growth and collapse of vapor bubbles. *Journal of Computational Physics* 187, 110–136. URL: <https://www.sciencedirect.com/science/article/pii/S0021999103000871>, doi:[https://doi.org/10.1016/S0021-9991\(03\)00087-1](https://doi.org/10.1016/S0021-9991(03)00087-1).
- 908
909
910
911
- 912 [52] Sussman, M., Almgren, A.S., Bell, J.B., Colella, P., Howell, L.H., Welcome, M.L., 1999. An adaptive level set approach for incompressible two-phase flows. *Journal of Computational Physics* 148, 81 – 124. URL: <http://www.sciencedirect.com/science/article/pii/S002199919896106X>, doi:<https://doi.org/10.1006/jcph.1998.6106>.
- 913
914
915
916
- 917 [53] Sussman, M., Puckett, E.G., 2000. A coupled level set and volume-of-fluid method for computing 3d and axisymmetric incompressible two-phase flows. *Journal of Computational Physics* 162, 301–337. URL: <http://www.sciencedirect.com/science/article/pii/S0021999100965379>, doi:[http://dx.doi.org/10.1006/jcph.2000.6537](https://doi.org/10.1006/jcph.2000.6537).
- 918
919
920
921
- 922 [54] Sussman, M., Smereka, P., Osher, S., 1994. A level set approach for computing solutions to incompressible two-phase flow. *Journal of Computational Physics* 114, 146 – 159. URL: <http://www.sciencedirect.com/science/article/pii/S0021999184711557>, doi:[http://dx.doi.org/10.1006/jcph.1994.1155](https://doi.org/10.1006/jcph.1994.1155).
- 923
924
925
926
- 927 [55] Sussman, M., Smith, K., Hussaini, M., Ohta, M., Zhi-Wei, R., 2007. A sharp interface method for incompressible two-phase flows. *Journal of Computational Physics* 221, 469–505. URL: <https://www.sciencedirect.com/science/article/pii/S0021999106002981>, doi:<https://doi.org/10.1016/j.jcp.2006.06.020>.
- 928
929
930
931

- 932 [56] Tanguy, S., Ménard, T., Berlemont, A., 2007. A level set method for
 933 vaporizing two-phase flows. *Journal of Computational Physics* 221, 837–
 934 853.
- 935 [57] Tatebe, O., 1993. The multigrid preconditioned conjugate gradient method,
 936 in: NASA. Langley Research Center, The Sixth Copper Mountain Confer-
 937 ence on Multigrid Methods, Part 2.
- 938 [58] Taylor, G.I., 1932. The viscosity of a fluid containing small drops of another
 939 fluid. *Proceedings of the Royal Society of London A: Mathematical, Phys-
 940 ical and Engineering Sciences* 138, 41–48. doi:[10.1098/rspa.1932.0169](https://doi.org/10.1098/rspa.1932.0169).
- 941 [59] Taylor, G.I., 1934. The formation of emulsions in definable fields of flow.
 942 *Proceedings of the Royal Society of London A: Mathematical, Physical and*
 943 *Engineering Sciences* 146, 501–523. doi:[10.1098/rspa.1934.0169](https://doi.org/10.1098/rspa.1934.0169).
- 944 [60] Unverdi, S.O., Tryggvason, G., 1992. A front-tracking method
 945 for viscous, incompressible, multi-fluid flows. *Journal of Computa-
 946 tional Physics* 100, 25 – 37. URL: <http://www.sciencedirect.com/science/article/pii/002199919290307K>, doi:[http://dx.doi.org/10.1016/0021-9991\(92\)90307-K](http://dx.doi.org/10.1016/0021-9991(92)90307-K).
- 949 [61] Wang, A., Evans, G., Mitra, S., 2023. A review of bubble
 950 surface loading and its effect on bubble dynamics. *Miner-
 951 als Engineering* 199, 108105. URL: <https://www.sciencedirect.com/science/article/pii/S089268752300119X>, doi:<https://doi.org/10.1016/j.mineng.2023.108105>.
- 954 [62] Wang, Z., Shi, D., Zhang, A., 2015. Three-dimensional lattice boltz-
 955 mann simulation of bubble behavior in a flap-induced shear flow. *Com-
 956 puters & Fluids* 123, 44 – 53. URL: <http://www.sciencedirect.com/science/article/pii/S0045793015003199>, doi:<https://doi.org/10.1016/j.compfluid.2015.09.007>.
- 959 [63] Wei, Y.K., Qian, Y., Xu, H., 2012. Lattice boltzmann simulations
 960 of single bubble deformation and breakup in a shear flow. *The Jour-
 961 nal of Computational Multiphase Flows* 4, 111–117. URL: <https://doi.org/10.1260/1757-482X.4.1.111>, doi:[10.1260/1757-482X.4.1.111](https://doi.org/10.1260/1757-482X.4.1.111), arXiv:<https://doi.org/10.1260/1757-482X.4.1.111>.
- 964 [64] Wong, A., Park, C., 2012. A visualization system for observing
 965 plastic foaming processes under shear stress. *Polymer Testing*
 966 31, 417–424. URL: <https://www.sciencedirect.com/science/article/pii/S0142941811002169>, doi:<https://doi.org/10.1016/j.polymertesting.2011.12.012>.
- 969 [65] Yoshikawa, H.N., Zoueshtiagh, F., Caps, H., Kurowski, P., Petitjeans, P.,
 970 2010. Bubble splitting in oscillatory flows on ground and in reduced gravity.
 971 *The European Physical Journal E* 31, 191–199.

- 972 [66] Zhang, J., Miksis, M.J., Bankoff, S.G., 2006. Nonlinear dynamics of
973 a two-dimensional viscous drop under shear flow. Physics of Fluids
974 18. URL: <http://scitation.aip.org/content/aip/journal/pof2/18/7/10.1063/1.2222336>, doi:<http://dx.doi.org/10.1063/1.2222336>.
- 976 [67] Zhang, J., Ni, M.J., Magnaudet, J., 2021a. Three-dimensional dynamics
977 of a pair of deformable bubbles rising initially in line. part 1. moderately
978 inertial regimes. Journal of Fluid Mechanics 920, A16.
- 979 [68] Zhang, J., Ni, M.J., Magnaudet, J., 2022. Three-dimensional dynamics of
980 a pair of deformable bubbles rising initially in line. part 2. highly inertial
981 regimes. Journal of Fluid Mechanics 943, A10.
- 982 [69] Zhang, J., Shu, S., Guan, X., Yang, N., 2021b. Regime map-
983 ping of multiple breakup of droplets in shear flow by phase-field
984 lattice boltzmann simulation. Chemical Engineering Science 240,
985 116673. URL: <https://www.sciencedirect.com/science/article/pii/S0009250921002384>, doi:<https://doi.org/10.1016/j.ces.2021.116673>.
- 988 [70] Zhang, W., Almgren, A., Beckner, V., Bell, J., Blaschke, J., Chan, C.,
989 Day, M., Friesen, B., Gott, K., Graves, D., Katz, M., Myers, A., Nguyen,
990 T., Nonaka, A., Rosso, M., Williams, S., Zingale, M., 2019. AMReX: a
991 framework for block-structured adaptive mesh refinement. Journal of Open
992 Source Software 4, 1370. URL: <https://doi.org/10.21105/joss.01370>,
993 doi:10.21105/joss.01370.